SANDIA REPORT
SAND2000-0152
Unlimited Release
Printed February 2000

Agile Dry Etching of Compound Semiconductors for Science-Based Manufacturing Using In-Situ Process Control

C. I. H. Ashby, G. A. Vawter, W. J. Zubrzycki,
W. G. Breiland, L. A. Bruskas, J. R. Woodworth, and
G. A. Hebner

Prepared by
Sandia National Laboratories
Albuquerque, New Mexico 87185 and Livermore, California 94550

Sandia is a multiprogram laboratory operated by Sandia Corporation,
a Lockheed Martin Company, for the United States Department of
Energy under Contract DE-AC04-94AL85000.

A disclosure of invention relating to the subject of this publication
has been filed with the U.S. Department of Energy.

Sandia National Laboratories

Issued by Sandia National Laboratories, operated for the United States Department of Energy by Sandia Corporation.

Available to DOE and DOE contractors from
U.S. Department of Energy
Office of Scientific and Technical Information
P.O. Box 62
Oak Ridge, TN 37831

Telephone: (865)576-8401
Facsimile: (865)576-5728
E-Mail: reports@adonis.osti.gov
Online ordering: http://www.doe.gov/bridge

Available to the public from
U.S. Department of Commerce
National Technical Information Service
5285 Port Royal Rd
Springfield, VA 22161

Telephone: (800)553-6847
Facsimile: (703)605-6900
E-Mail: orders@ntis.fedworld.gov
Online order: http://www.ntis.gov/ordering.htm

SAND2000-01521
Unlimited Release
Printed February 2000

Agile Dry Etching of Compound Semiconductors for Science-Based Manufacturing Using In-Situ Process Control

Carol I.H. Ashby, G. Allen Vawter, and Walter J. Zubrzycki
Semiconductor Materials and Processes Department

William G. Breiland and Larry A. Bruskas
Chemical Processing Science Department

Joseph R. Woodworth and Gregory A Hebner
Laser, Optics, and Remote Sensing Department

Sandia National Laboratories
P.O. Box 5800
Albuquerque, NM 87185-0603

Abstract

In-situ optical diagnostics and ion beam diagnostics for plasma-etch and reactive-ion-beam etch (RIBE) tools have been developed and implemented on etch tools in the Compound Semiconductor Research Laboratory (CSRL). The optical diagnostics provide real-time end-point detection during plasma etching of complex thin-film layered structures that require precision etching to stop on a particular layer in the structure. The Monoetch real-time display and analysis program developed with this LDRD displays raw and filtered reflectance signals that enable an etch system operator to stop an etch at the desired depth within the desired layer. The ion beam diagnostics developed with this LDRD will permit routine analysis of critical ion-beam profile characteristics that determine etch uniformity and reproducibility on the RIBE tool. This is the final report for LDRD #3506.520.

Contents

Program Objective

Many different materials with greatly varying etching characteristics are used in the fabrication of compound semiconductor devices, microelectromechanical systems (MEMS) , and on-wafer chemical analytical systems ("Chem-Lab-on-a-Chip"). Highly reproducible and quickly re-established standard etch processes for each material are essential. However, when a single tool must be used for processing a wide range of materials using very different process chemistries, reliable etch performance can be very challenging to achieve. The objective of this LDRD was the development and routine implementation of in-situ diagnostics that permit real-time measurements of plasma etching behavior to provide excellent control and reproducibility despite changes in materials and etch chemistries in a given tool.

Program Accomplishments

1) In-situ optical Diagnostics

We have developed a data collection program (Monoetch) that records a single-wavelength reflectance signal during plasma etching. Because substrates are usually patterned with photoresist, the ADVISOR methods that calculate deposition rates in MBE and MOCVD applications are not useful in etching. Thus, we have used more empirical methods for determining endpoints during the etch process.

The reflectance signal includes the plasma emission background, a long-period oscillation due to slow etching of photoresist, higher-frequency oscillations from the thin-film structure being etched, and noise. Monoetch program disentangles these patterns using digital filtering methods. It displays the raw reflectance signal along with three waveforms that have been filtered with the following constraints:

a. A photoresist bandpass filter removes high-frequency noise and interference oscillations from the thin film structure, leaving an oscillation that largely represents the interferogram that would result from etching photoresist (PR) alone. Given the PR refractive index, the PR etch rate may be determined from this waveform.

b. A thin-film bandpass filter removes background, drifts, photoresist oscillations, and high-frequency noise. The resultant waveform represents the interferogram that would result from etching an un-patterned thin-film structure. Layers may be identified by their characteristic oscillations, and interfaces are often seen as kinks in the waveform due to instantaneous phase shifts that occur at interfaces.

c. An Interface Detector smoothing second-derivative filter helps identify interface kinks by displaying singularities in the second derivative of the waveform that occur whenever there is a discontinuous change in slope.

These filters may be adjusted interactively to see their effect on the waveform. Two digital filtering methods are being explored. A finite impulse response (FIR) method presents an updated data point that is centered in a filter window. This method presents stable, filtered waveforms, but can only display filtered data information that occurred at times prior to half the data window. A fast fourier transform (FFT) method presents a filtered waveform over the entire data range, including the most recently acquired data, but the recent data is distorted by Gibbs oscillation artifacts.

A playback feature allows filtering of a stored data file to optimize an endpoint detection scheme. It can also display the time-reversed interferogram from a deposition experiment that used the Monogrow program to record an in-situ reflectance signal during growth of the thin film structure.

To accommodate the unavoidable uncertainty in obtaining an un-phase-shifted filtered waveform in real time, we are experimenting with a simple predictor method. By detecting two easily-identified reflectance features in the structure, it determines the etch rate in real time and forecast when the endpoint will occur.

2) Ion Beam Diagnostics

We have measured spatially resolved beam divergence in the RIBE system. These were the first ever for a broad ion beam source. We gained a better understanding of grid form factor issues and accelerator grid bias selection. We determined that the beam energy spectrum follows the set points well. These data determined the type of tool that would give the best benefit/cost ratio if installed permanently in our RIBE system. We concluded that a linear Faraday-cup array could be built using the same technology as the spectrum analyzer and that such an array could be made to fit in existing ports with the sample stage in place. The Faraday cup array has been built and control software is being written. The final tool will allow real-time display of the ion beam uniformity across the sample diameter. We will use this display to optimize the ion beam uniformity or divergence without resorting to time-consuming wafer-etch trials. We also expect to be able to monitor the etch system for grid wear, as manifested by long-term drift of the ion beam profile. Such in-situ measurements of beam quality will allow us to improve diagnosis and prediction of needed repairs BEFORE they are evident as out-of-spec etches.

Appendix A

Publications

G. Allen Vawter, Joseph R. Woodworth and Walter J. Zubrzycki, " Spatially-Resolved Ion Trajectory Measurements During Cl_2 Reactive Ion Beam Etching and Ar Ion Beam Etching", to be published in Journal of Vacuum Science and Technology.

Walter J. Zubrzycki, G. Allen Vawter, and Joel R. Wendt, "High-Aspect-Ratio Nanophotonic Components Fabricated by Cl_2 RIBE Beam Etching and Ar Ion Beam Etching", to be published in Journal of Vacuum Science and Technology.

Presentations

G. Allen Vawter, Joseph .R. Woodworth, Walter J. Zubrzycki , " Spatially-Resolved Ion Trajectory Measurements During Cl2 RIBE and Ar IBE (Invited Paper)".
Presented at the 43rd International Conference on Electron, Ion, and Photon Beam Technology and Nanofabrication, Marco Island, FL, June 1-4, 1999.

Walter J. Zubrzycki, G.Allen Vawter, Joel R. Wendt, "Influence of Ion Beam Divergence and Chamber Pressure on High-Aspect Ratio Nanophotonic Components by Cl_2 RIBE."
Presented at the 43rd International Conference on Electron, Ion, and Photon Beam Technology and Nanofabrication, Marco Island, FL, June 1-4, 1999.

Appendix B

Monoetch 2.0

A program to record real-time *in situ*
reflectance waveforms during thin
film etching

William G. Breiland
wgbreil@sandia.gov

Larry Bruskas
labrusk@sandia.gov
Sandia National Laboratories

Table of Contents

Using This Document

This document comes as an Adobe® Acrobat® 4.0 ".pdf" file, and can be viewed with any computer operating system using "Acrobat Reader", which is available for free from the website: http://www.adobe.com/prodindex/acrobat/readstep.html#reader. Online viewing allows one to take advantage of the bookmarks and links (links are indicated with a thin blue rectangular box) imbedded within the text to quickly jump to various sections simply by clicking on the bookmark or link. Web page links within the document are also active, allowing the system to direct a browser to the web page listed in the Acrobat document. A printed copy of the document may be obtained with the "print" command within the Acrobat Reader. Various "Views" are available within the reader to make online reading easier. The hierarchical arrangement of bookmark headings that appears on the left hand side of the document may be toggled on and off with the "show/hide navigation pane" icon on the taskbar. The user also has access to the full text search capabilities of Acrobat Reader.

Overview

This section provides an overview of what Monoetch is and what features it has. Actual use of the program is detailed in the section Using Monoetch.

Monoetch records a real-time, *in situ* waveform of single-wavelength reflectance vs. time during the etching of thin films. It can be used as a stand-alone data collection system or can be integrated into the process with user interaction.

The reflectance experiment for growing films

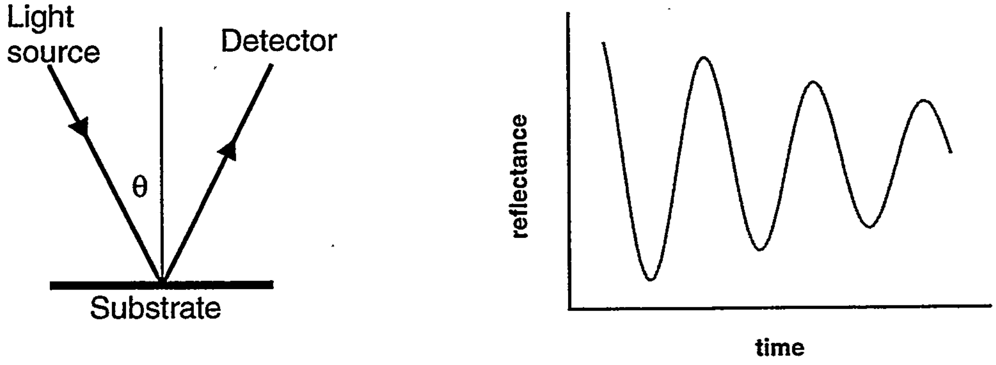

Fig. 1 Reflectance experiment with monochromatic light and the interference oscillations that result when monitoring during the growth of a thin film.

Pictured in Fig. 1 is a schematic of a simple reflectance experiment and the waveform that results when reflectance is recorded during thin film *growth*. The oscillations result when light reflected from the substrate interferes with light reflected from the top of the semi-transparent film.

The oscillations decay if the film absorbs light. Oscillations will be observed only if monochromatic light is used. This may be accomplished with either a laser source or a broadband source and a narrowband (~10 nm) filter in front of the detector. Interference will be observed in films whose thickness does not exceed the "coherence length" of the light, defined to be $\lambda^2 / n\Delta\lambda$, where λ is the vacuum wavelength of light, $\Delta\lambda$ is the bandwidth of the interference filter, and n is the real part of the refractive index of the film.

The frequency of the oscillations depends on the wavelength of light, λ, the angle of incidence, θ, the complex refractive index, $N = n - ik$, where n and k are the optical constants of the film, and the growth rate of the film. The amplitude of the oscillation depends on the polarization of the detected light ("*p*" has the electric field vector parallel to the plane of incidence, and "*s*" has the electric field perpendicular to the plane of incidence), the complex refractive index, and the amplitude and phase of light reflected from underlying films and the substrate. The waveform is not a pure sinusoid, but typically has alternating rounded and cusp-like extrema. This complex reflectance behavior is easily modeled. By fitting the measured reflectance waveform to the model, it is possible to extract the growth rate and the optical constants of the film as adjustable parameters. The fitting procedure has been dubbed ADVISOR for Analysis of Deposition using Virtual Interfaces and Spectroscopic Optical Reflectance. This analysis has been extensively used with the Sandia-developed software package, AADVISOR 2.0, to greatly improve MOCVD and MBE process yield and accuracy.

The reflectance experiment for etching thin-film structures

In principle, optical monitoring of a device structure grown with MOCVD or MBE yields a waveform that is essentially the "time-reversed" image of the growth reflectance waveform. Figure 2 illustrates this behavior by comparing the time-reversed reflectance waveform from a growing thin film structure with the *in situ* reflectance signal of the same structure during etching in an ICP reactor. Pauses in the growth process of course are not seen in the etching waveform, but otherwise the two profiles look substantially the same. This would lead one to believe that determining etch rates is as simple as applying ADVISOR methods and extracting a "negative" growth rate.

Unfortunately, practical applications of etching yield a more complicated situation. The purpose of etching is to selectively remove parts of the thin film structure by patterning with photoresist. As a result, the surface of the wafer to be etched is no longer smooth. The presence of spatially-varying patterns presents run-to-run differences in the amount of exposed surface contained within the reflectance spot size. As a result, it is virtually impossible to obtain an absolute reflectance from the wafer prior to or during etching. Because ADVISOR requires an absolute reflectance to be effective, this presents a serious challenge to the straightforward implementation of ADVISOR as a negative growth rate measuring tool.

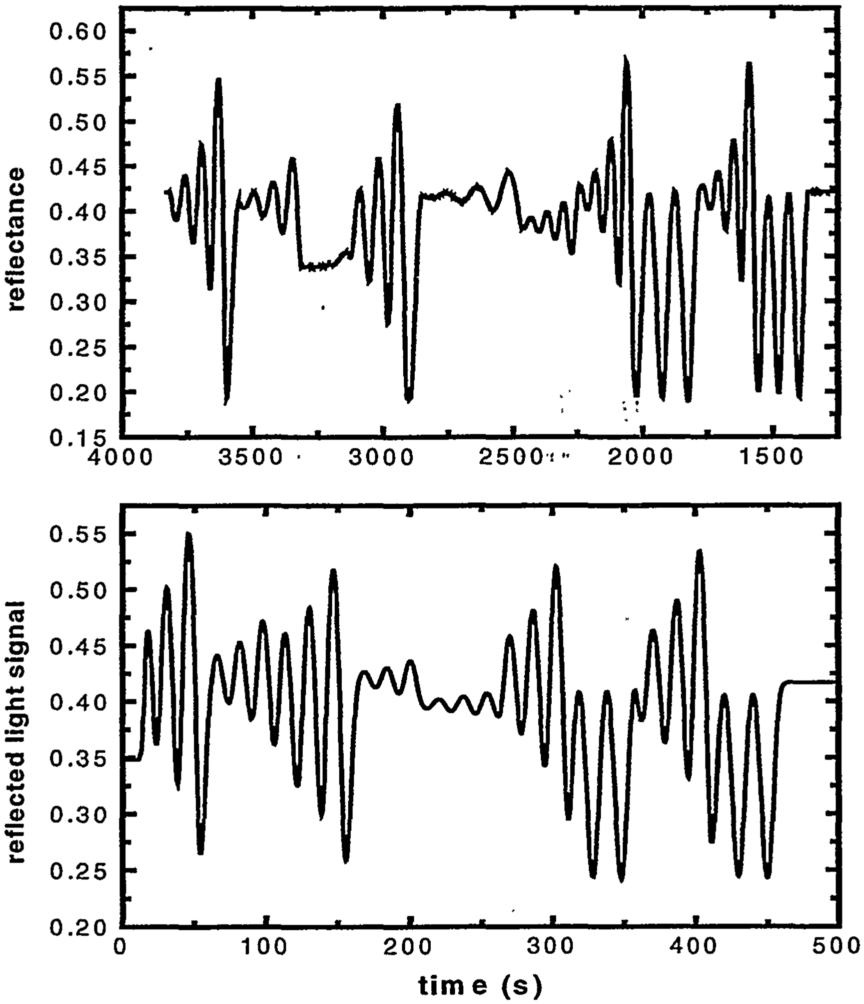

Fig 2: Top: in situ reflectance of thin film structure grown at 750 °C (note reversal of time axis). Bottom: in situ reflectance signal from the same structure as it is etched at room temperature by an ICP process. Note that etching is accomplished in roughly one third the time required for growth. Pauses in the growth run are not seen in the etching waveform.

Theoretical investigations of the reflectance from rough thin-film structures has revealed another difficulty. It is straightforward to model the reflectance oscillations from a surface containing a distribution of multiple-layer thin film structures with different thicknesses. However, analysis shows that the virtual interface concept, which so readily applies to smooth surfaces in ADVISOR techniques, cannot be used for patterned films. Each area in the patterned wafer leads to a distinct virtual interface reflectance. As a result, it is impossible to perform a least-squares fit of a reflectance waveform to extract a single value of the virtual interface as is done with ADVISOR.

Yet another complication exists when *in situ* reflectance monitoring is used for etching applications. As shown in Fig. 3 below, an additional low-frequency oscillation is often observed to mix with the interference oscillations expected from the thin film structure. The low-frequency component comes from interference oscillations arising from a slow etching of the photoresist that is used to mask the wafer. This interference makes it difficult to identify features in the waveform that are associated with thin film structures.

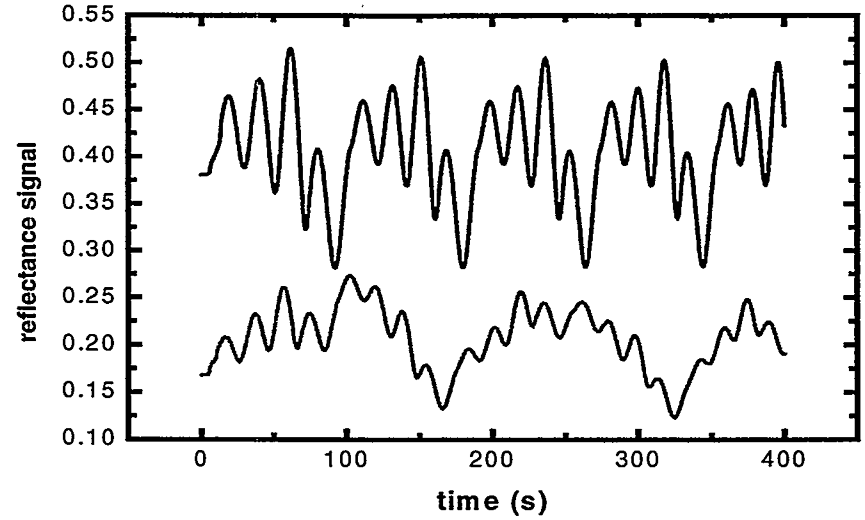

Fig 3: Top: Reflectance waveform from an un-patterned thin film structure during ICP etching. Bottom: Reflectance waveform from the same structure that has been patterned with photoresist. Etching of the photoresist adds additional low-frequency components to the waveform, making it difficult to determine the positions of interfaces and thin-film oscillations from the device structure.

In addition to the low frequency oscillations, the effective roughness of the surface increases as unmasked regions are etched away, yet masked regions remain at substantially the same height. This leads to a slow decrease in the signal over the time of the etch run.

As a result of the difficulties outlined above in providing a quantitative optical measure of etch rate, we have opted to take a more empirical approach to the problem in the Monoetch program. It is still very valuable to have a real-time, *in situ* monitor that tracks the progress of the process. The following section outlines the features that have been added to Monoetch as tools for interpreting the waveform.

Features supported by Monoetch

The central purpose of Monoetch is to record a reflectance waveform that is collected with an *in situ* reflectance probe. As such, it may be viewed simply as a stripchart recording program having customized features that integrate with an etching run. However, considerable value is added by making the data collection process address issues important to etching. Below is a quick synopsis of the custom features added to the Monoetch stripchart program to streamline its use.

Digital filters

The Monoetch program attempts to disentangle the mixed patterns from roughening, photoresist, and thin-film interference oscillations using digital filtering methods. During the run, the user is presented with displays of the raw reflectance signal along with three waveforms that have been filtered with the following constraints:

1. A "photoresist" bandpass filter is applied that eliminates the background signal and any slow drifts toward higher or lower reflectance values. It filters out high-frequency noise and the interference oscillations from the thin film structure, leaving an oscillation that largely represents the interferogram that would result from etching a film of photoresist. If the refractive index of the photoresist is known, the photoresist etch rate may be determined from this waveform.
2. A "thin-film" bandpass filter is applied that removes background, drifts, and photoresist oscillations. High-frequency noise is filtered out as well. This leaves a waveform that largely represents the interferogram that would result from etching of an un-patterned substrate with a thin-film structure. Layers may be identified by their characteristic oscillations, and interfaces are often seen as "kinks" in the waveform due to instantaneous phase shifts that occur at interfaces.
3. An "Interface Detector" smoothing second-derivative filter is applied to help identify interface "kinks" by displaying singularities in the second derivative of the waveform that occur whenever there is a discontinuous change in slope.

All the above filters may be adjusted interactively to see their effect on the waveform. Two digital filtering methods are implemented. A finite impulse response (FIR) method presents an updated data point that is centered in a filter window. This method presents stable, filtered waveforms, but can only display filtered data information that occurred at times prior to half the data window. A fast Fourier transform (FFT) method presents a filtered waveform over the entire data range, including the most recently acquired data, but the recent data is distorted by Gibbs oscillation artifacts. The user may choose either FIR or FFT filtering to best suit a specific application.

Playback of datafiles

Monoetch has been given a "playback" feature that allows one to fetch a previously recorded data file and experiment with various filter combinations to optimize a desired endpoint detection scheme. The user may run through an experiment in real time to test various endpoint scenarios, and fast forward or reverse to critical parts of the data file. This feature is particularly useful with a "calibration run" in which a sample is sacrificed to etch completely through an endpoint. The reflectance data from this sample is then used in playback simulations to develop a viable endpoint detection procedure.

Reversed display of reflectance from growth runs

Monoetch is capable of displaying the time-reversed interferogram from a deposition experiment that used the Monogrow program to record an in situ reflectance signal during growth of the thin film structure. If the same wavelength is used for monitoring etching, then one expects to see similar features from a time-reversed growth run in an etching run.

Endpoint predictor and countdown timer

To accommodate the unavoidable uncertainty in obtaining an un-phase-shifted filtered waveform in real time, Monoetch has a simple endpoint predictor method. By marking two easily-identified interface or reflectance oscillation features in the structure prior to the desired endpoint, one can determine the etch rate in real time and forecast the time at which a desired endpoint will occur. Once the endpoint prediction has been determined, Monoetch displays an easily-read countdown timer to assist in stopping the etch run at the predicted endpoint.

Using Monoetch

Double-clicking the Monoetch icon brings up the main GUI display pictured below. Monoetch looks for a "configuration file" with an extension .cfg (see The .cfg file) to load the program with settings that were saved from a previous session. More than one configuration file may be used with Monoetch. If more than one file is found in the Monoetch folder, then a file select dialog box is presented to allow the user to select one of the configuration files. This allows one to save and recall custom filter settings for specific device structures. If only one .cfg file is in the folder, Monoetch will load it without displaying the file select dialog. After reading the .cfg file, initializations are done and the program is ready to take data.

The large graph displays a full-scale version of any of the "thumbnail" graphs displayed on the right side of the panel. To display any thumbnail data in the large main graph, click on that thumbnail graph. Each thumbnail displays filtered reflectance data. The filters are designed to bring out various features in the reflectance waveform. From top to bottom, the filters are labeled Interface Detector, Photoresist Oscillations, Thin Film Oscillations, and Reflectance Signal.

The Interface Detector is a bandpass second derivative filter. Its purpose is to filter out both photoresist and thin film oscillations and display the second derivative of what remains. At thin film interfaces, the reflectance signal typically undergoes discontinuous phase shifts. Thus the reflectance waveform exhibits sharp changes in slope at interfaces. These kinks will produce singularities in the second derivative, giving "spike" features.

The Photoresist filter is just a low-pass filter that removes noise and thin-film interference oscillations, leaving the reflectance waveform caused by etching of the photoresist.

The Film Oscillations filter is a highpass filter that rejects the long-period photoresist oscillations and displays the oscillations that result from thin film interference.

The Reflectance graph is just a display of the raw reflectance data. It is smoothed by the action of compressing the raw data array into a 512-point graph array.

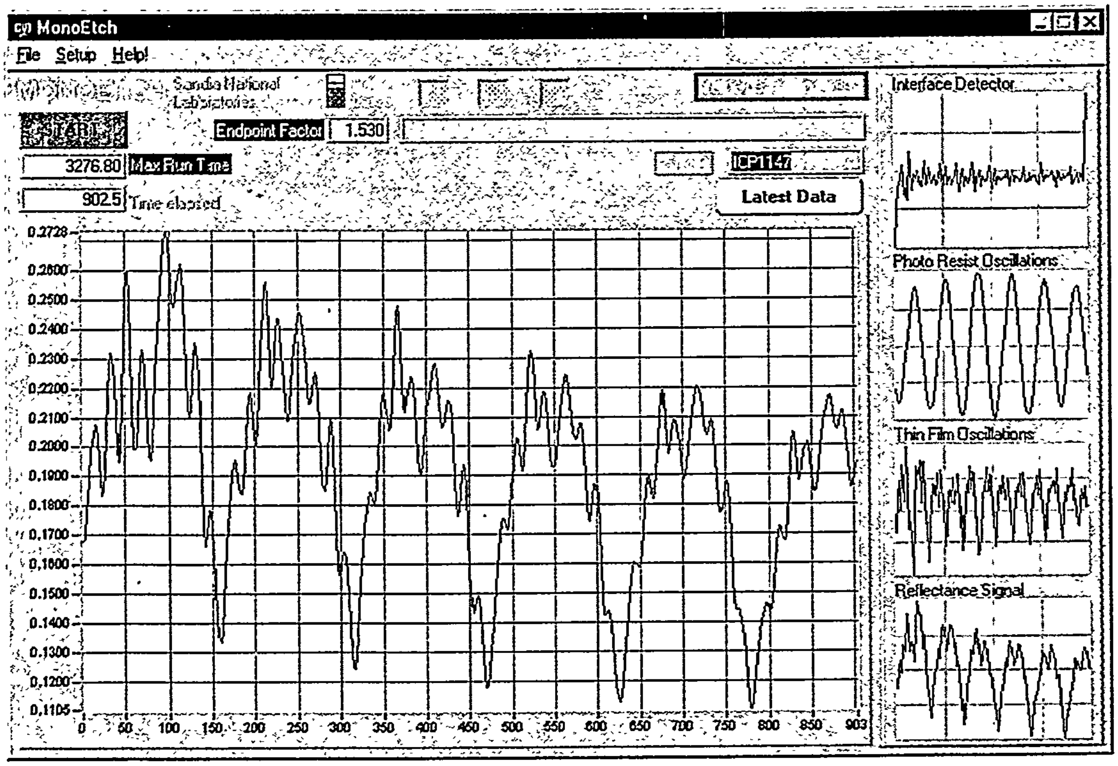

Endpoint Factor 1.530

3276.80 Max Run Time

902.5 Time elapsed

NOTE: ***Context-sensitive help for any object in the program window may be fetched by right-mouse clicking on the object.***

Initial signal

In day-to-day operation, one simply verifies that the signal is at a reasonable starting level and then presses START to begin data collection. The reflectance signal value is checked by selecting Setup -> Signal Display from the menu bar, or by using the keyboard shortcut "CTL-S". This brings up the panel display shown below.

The top LED display gives the signal strength in normalized units, where 0 is no signal and 1 is full scale for the device that is recording the signal. It is important to adjust the signal level using the Sig Gain control to an appropriate value. If the signal is too small, resolution will be lost and the data will be noisier than it would be with a higher gain setting. If the signal is too big, reflectance changes during growth could cause the signal to rise to beyond full scale, at which point data is lost. If changes in reflectance cause the signal to exceed full scale in the hardware, the observed reflectance will "peg" at a constant maximum value.

The middle and bottom displays provide information on the stability of the signal as an absolute and percent standard deviation. The number of points used to determine these statistics can be changed with the StdDev Samples control.

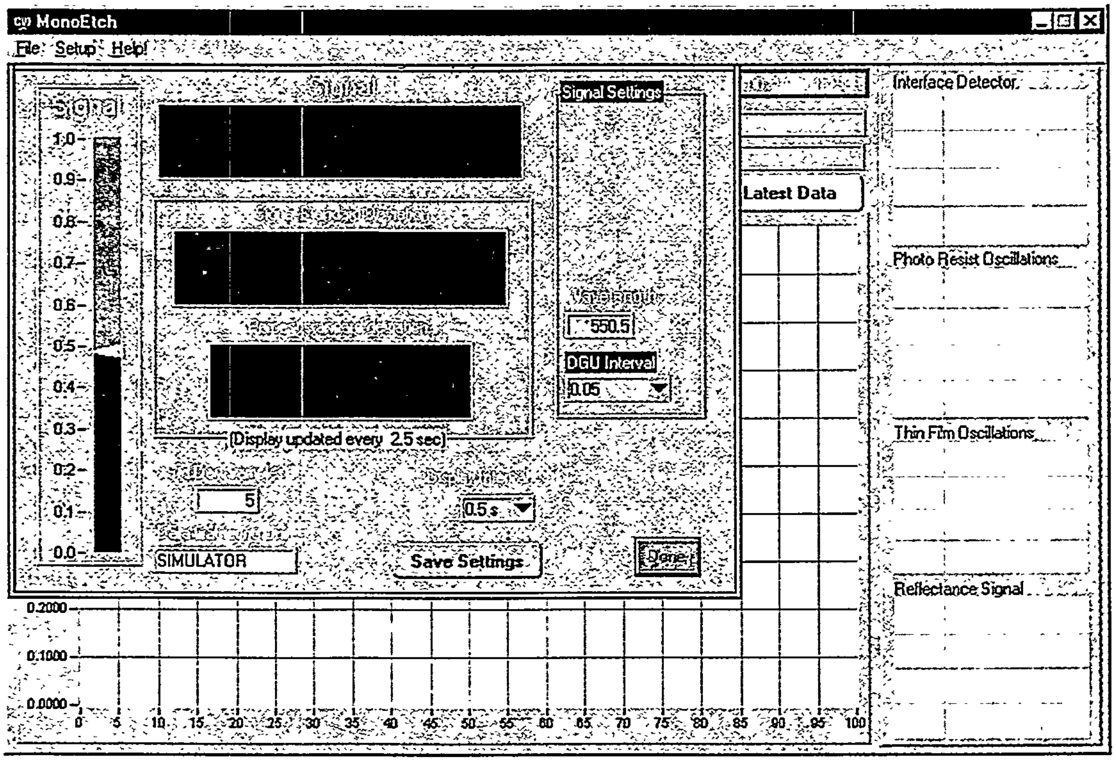

This panel also allows the user to adjust the time intervals for collecting and displaying the data using the DGU Interval and Display Interval controls, respectively. See the descriptions in **Display Signal (shortcut CTL-S)** for further details.

Data collection

Once the initial signal is deemed adequate, data collection is started by pressing the START button on the left of the main panel. As data is collected, the raw reflectance signal is displayed in the main graph and the four thumbnail graphs display filtered data. To examine any of the filtered data more closely, click on the thumbnail and the data in the thumbnail will be displayed in the main graph.

To look at the most recent data more closely, click on the Latest Data control. A popup graph displaying the latest n points, where n can be 50, 100, or 200 is placed in the upper left of the main graph display. Alternatively, a zoomed display of any portion of the data may be examined by "lassoing" a section of the data. (To do this, the program must be put into Lasso mode with the Hot/Lasso switch.) Drag the cursor over the features to be zoomed. When the mouse is released, the main display "freezes" and displays a zoomed plot of the data enclosed in the dragged zoom rectangle. Two cursors are also provided, along with a popup panel that allows the user to measure the time that a feature has occurred, time differences between features, and the ability to set endpoint markers (see Endpoint Prediction for a detailed description of the endpoint prediction utilities). Double-clicking the main display will reset it to full scale and dynamic updating.

Endpoint markers may also be set during the run. By selecting Hot in the Hot/Lasso switch, endpoint markers may be set by clicking on any feature in either the main or Latest Data graph. Alternatively, the markers may be set by clicking in the "M#" check box. The marker is set to the time that the box was clicked.

Data collection is stopped by clicking on the button used to start the run. A file with a root name provided in the Run ID control is saved with a ".tsb" extension. (See Data file format for an explanation of data file formats).

Endpoint Prediction

Monoetch has a simple utility for predicting endpoints, based either on previous experience with a calibration run, or based on knowledge of the thickness of the films that are being etched. The method is based on the following procedure, illustrated in Fig. 4. This figure shows a second-derivative plot of a reflectance waveform that etches through a DBR mirror structure consisting of alternating layers of high and low index quarter-wave stacks. Suppose that the desired endpoint is midway into the third high-index layer, marked by the arrow labeled "ep". Because the etch rate is known to vary slightly over the course of the run, features near the endpoint are chosen for relative etch rate calibration. The positive spike marked "M1" and the negative spike, marked "M2" are chosen. Monoetch automatically uses the difference in time between M1 and M2, combined with a user-supplied endpoint factor, *EF*, (entered in the Endpoint Factor box in the main window) to calculate an endpoint time with the formula:

$$ep = EF(M2 - M1) + M3$$

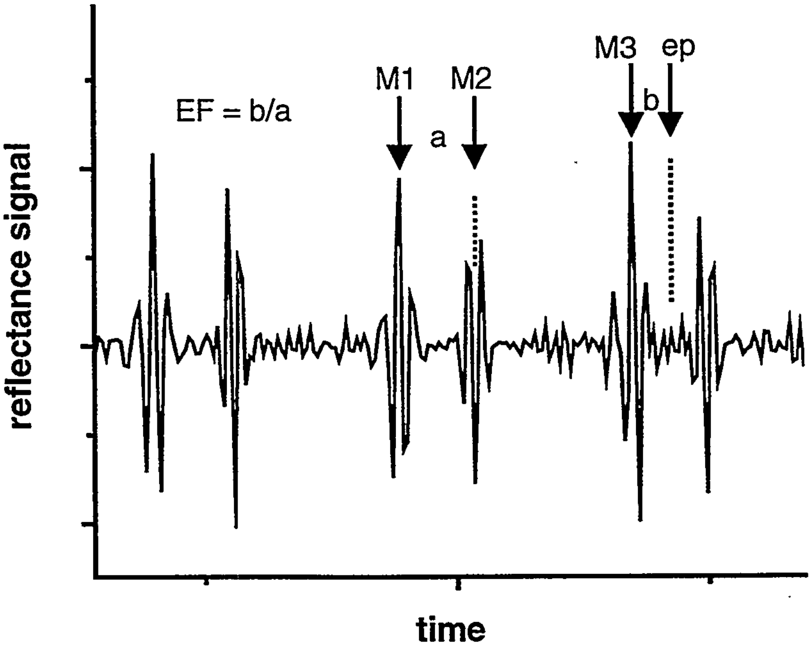

Fig 4: Illustration of endpoint prediction. Two features, M1 and M2, separated in time by **a**, are chosen to determine the relative etch rate. The desired endpoint, ep, is measured relative to a third feature, M3, separated in time by **b**. An "Endpoint Factor", EF = b / a is entered into Monoetch before the run. M1, M2, and M3 are marked by the user during the run. After M3 is marked, ep is calculated and a countdown timer is displayed in the Monoetch window.

The Endpoint Factor, *EF*, is determined before the run in either of two ways. In the present example, $a = (M2 - M1)$ marks the thickness of the high-index layer. The desired endpoint is halfway into the next high-index layer, so *EF* is just $b/a = 0.5a/a = 0.5$. Alternatively, a completely empirical endpoint factor may be established by performing a sacrificial run that purposely etches past the endpoint. The waveform from the sacrificial calibration run is used to establish a relative Endpoint Factor from ratios of times measured between features. By using the playback option and filter adjustments described in other parts of this manual, one may devise an empirical Endpoint Factor that is used to predict a stopping point for future runs on device structures.

The M3 marker may be "pre-checked" before M2 is established. If this is done, the countdown starts immediately after the user has notified Monoetch of the time for M2, i.e. $ep = EF\,(M2 - M1) + M2$. Note that this endpoint prediction scheme uses only relative etch rates, so absolute thickness values are not required.

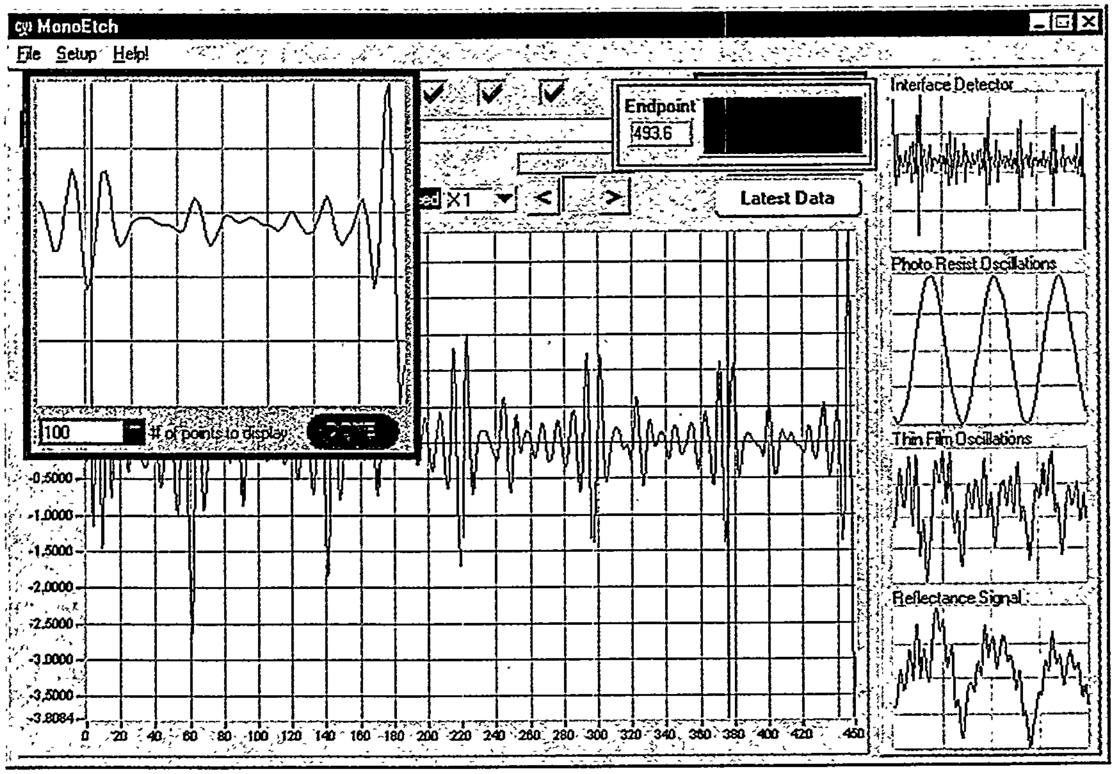

The figure above illustrates the use of markers and the countdown timer during a replay session. In a typical application, the Endpoint Factor is entered prior to the run, or a custom .cfg file is loaded with the Endpoint Factor and filter settings for a specific device structure. During the etch run, markers M1, M2, and M3 are set using the "Hot" cursor mode by clicking on a feature in the main display graph or in the Latest Data graph popup. When M3 is established, the countdown timer shown in the above figure is activated to help the operator determine the endpoint moment. It counts down to zero in green numerals, switching to negative red numerals after the predicted endpoint has been reached.

Menu Selections

File menu selections

Open...(shortcut: CTL-O)

This menu item allows the user to open a data file stored in the .tsb format. It can be used to recall a previous etching run or to look at reflectance waveforms from growth runs to display what might be expected in an etching run.

Replay...

This option allows a user to place a previous etching run into a playback recorder application as a tool for determining the optimum filter settings and endpoint schemes. A file select popup is opened to let the user select a data file, and the selected file is placed in memory. When the Start button is pressed, four playback controls appear. The "Playback Controller" icons follow standard conventions used in CD and tape players. The "<" and ">" buttons replay the data in the reverse and forward directions, respectively. The square button between the forward and reverse buttons pauses the replay action. The "Replay Speed" ring control allows the user to speed up the replay action up to X100 in order to "fast-forward" to a desired part of the waveform. Filter settings may be adjusted when the replay is paused. The endpoint predictor markers are fully operational in replay mode. To aid in endpoint detection, a magenta vertical cursor is displayed in the main and recent data graphs after the endpoint countdown timer passes zero. This allows the user to try out various endpoint determination schemes on a sample that has been purposely over-etched.

Reverse Plot

This utility reverses the time axis on data that has been fetched with the Open... command. It is intended to reverse the reflectance display from a Monogrow growth run to make it easier to see what the basic shape of the etching waveform will be. A typical use of this option is to Open the Monogrow file, Reverse Plot, then Print Screen.

Save Settings

This creates a ".cfg" file record of all the program settings. This feature allows one to save any number of .cfg files with customized filter, Endpoint Factor, and data collection settings to be used in specialized applications.

Print Screen (shortcut CTL-P)

This sends an image of the entire Monoetch window contents to the printer.

Quit

Exits the Monoetch program. Clicking on the standard **X** icon in the upper right corner of the Monoetch window will also exit the program.

Setup menu selections

Display Signal (shortcut CTL-S)

This brings up a panel that displays the raw input signal from the reflectance unit and a number of controls used to determine how data is stored and displayed. It is wise to use this panel prior to an etching run to verify that a reasonable noise-free signal is being received prior to the start of data collection. The panel also holds the following controls:

- Gain or Sensitivity: This selects a value that controls the size of the signal from the reflectance "Data Gathering Unit". Value of the control depends on hardware used.
- DGU Interval: This sets the time interval between data collection events from the "Data Gathering Unit" (DGU). This time typically is shorter than the Display Interval, which determines how often the raw data is displayed and filtered in the Monoetch display. The DGU Interval also determines the

maximum time that data can be collected with a run. A maximum of 65535 points can be stored in a compressed .tsb file (see Data file format), so the maximum run time is given by 65535 * `DGUinterval`. A value for the interval should be chosen that provides a reasonable maximum run time, yet is fast enough to store all significant changes in the reflectance signal.

- Display Interval: This sets the time between screen updates of the data display graphs. It typically is slower than the DGU Interval, which is the time between data collection events. When the FIR filter type is chosen, data is compressed from "DGU intervals" to "Display Intervals" before filtering. This compression reduces the extent of the filter and speeds up the filtering process.

Filter Settings (shortcut CTL-F)

This option brings up a panel that contains controls for setting filter cutoff and extent values for each of the three "thumbnail" graphs (see figure below). This section only describes the mechanics of implementing the filters within Monoetch. See **Digital filter methods** for an explanation of the algorithms used for data filtering. Settings may be made for each of the three types of filters used in Monoetch: Interface Detector, Photoresist filter, and Film oscillation filter. Each filter is selected by clicking on the appropriate thumbnail graph. If the Reflectance Signal graph is selected, the filter setup panel is disabled. Filter cutoff settings are in units of time, i.e. oscillation period. This helps one to set the values by using the differences in the times between features in the reflectance waveform. Extent settings are in units of data points. See the discussion in **Adjusting filter settings** for a guide to achieving the correct values.

The Filter Settings panel has the following controls:

- Short Cutoff: This sets the limit for attenuation of signals with short periods, i.e. high frequencies. Its main function is to remove noise or to isolate photoresist oscillations.
- Long Cutoff: This sets the limit for attenuation of signals with long periods, i.e. low frequencies. Its main function is to remove photoresist oscillations and to enhance "kinks" in the Interface Detector.
- Extent: This sets the extent of the filter. For FFT filter type, this gives the base of a triangular window applied in the 512 element array of the frequency spectrum. An extent of 10 applies a triangular window that starts with a value of 0 at the cutoff value and rises to 1 at 10 array index values from the cutoff index. For the FIR filter type, the extent gives the number of data points included to either side of the filtered point, i.e. the size of the filter window.
- FFT/FIR button: This selects the filter type. Each type has advantages and disadvantages, as discussed in **Digital filter methods**. Because the extent has a different meaning depending on filter type, switching filter types will cause the extents to be set to default values.
- Maximum Displayed Period: This control affects only the appearance of the Filters Settings controls. It is used to stretch or compress the range of periods displayed in the spectrum graph and cutoff controls.

- Spectrum Graph: This graph is display only. It plots the frequency spectrum of the raw reflectance data as a function of oscillation period. It is useful for identifying the long-period photoresist oscillation as a distinct peak from other shorter-period film oscillations. It is also useful for setting the short-period cutoff at a value just below any significant spectral feature to eliminate noise yet include meaningful film oscillations.

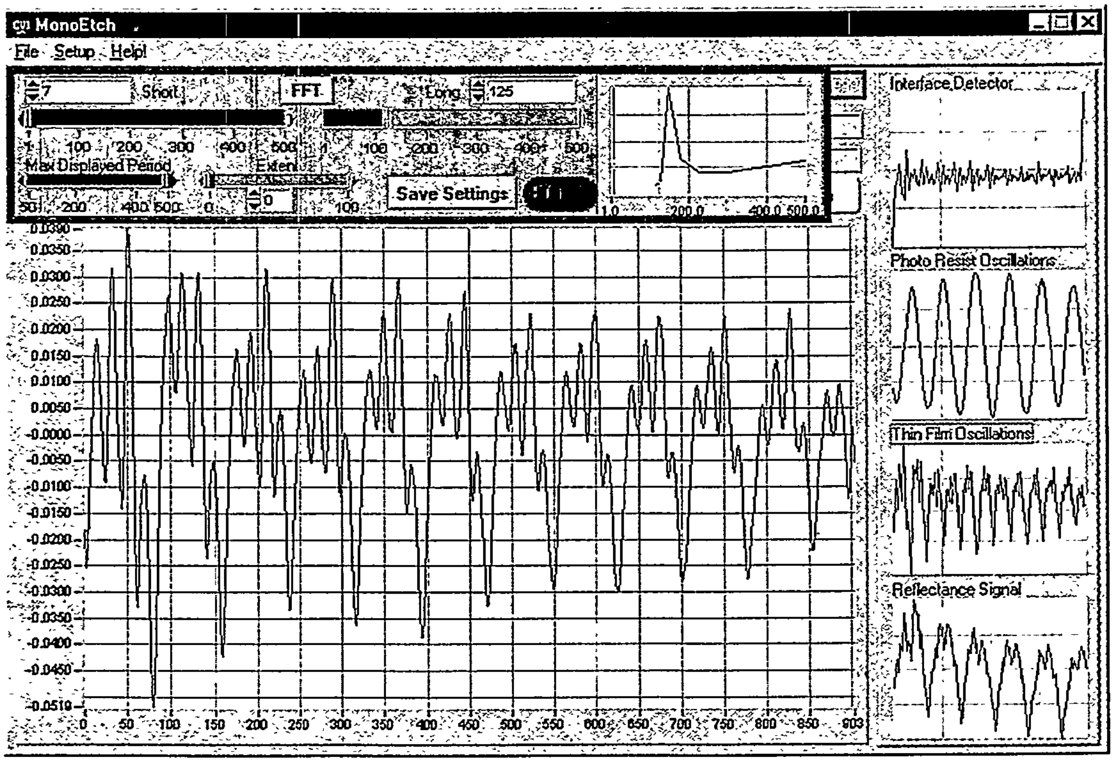

Note that the Interface Detector filter is a bandpass second derivative, and the other two filters are just bandpass filters. The ability to extract photoresist vs. film oscillations relies exclusively on the filter settings.

Adjusting filter settings

As described in the section, **Filter Settings (shortcut CTL-F)** above, filter cutoffs and extent may be adjusted interactively with the controls in the filter settings menu panel. This section provides a guide to setting the cutoffs to achieve a desired result.

The waveform power spectrum

A graph of the power spectrum of the reflectance waveform is shown in the filter settings panel. An example of such a spectrum, obtained by a fast Fourier transform of the waveform, is shown in Fig 5 below. Much of the spectral information is clustered at very low frequencies compared to the highest resolvable Fourier component. As a result, it is more convenient to plot the power spectrum as a function of oscillation period rather than oscillation frequency. This choice of x-axis also provides a direct connection between a spectral feature and its associated oscillation period in the waveform plot. For example, the longest-period spectral peak shown in the shaded section of Fig 5 corresponds to the photoresist oscillations. Its period of 150 s is directly manifested as a slow undulation of the etching waveform with a wavelength of 150 s.

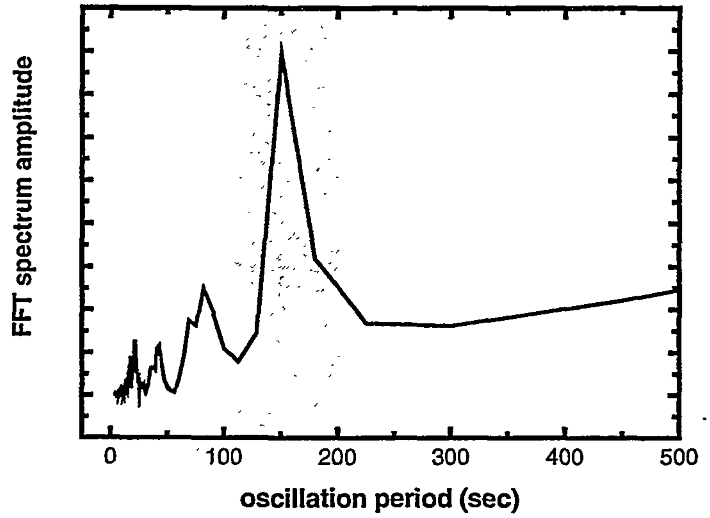

Fig 5: Power spectrum of an etching waveform, plotted as a function of the oscillation period. This choice of x-axis makes it easier to isolate and identify low-frequency (long period) oscillations. The strongest peak in the spectrum shown in the shaded region is due mostly to photoresist oscillations.

Filter cutoff adjustments

The waveform spectrum graph is used to identify cutoff positions for the filters. For example, to set the filter to isolate thin film oscillations, drag the slider switch on the Long cutoff control to roughly 100 s. A cursor in the graph plots the value of the slider as it is moved. The cursor may be positioned in the valley between the large photoresist peak and the next-highest peak, which is due to thin film oscillations. The Short cutoff control is positioned to include all meaningful spectral peaks, yet rejecting high-frequency noise. The extent slider is used to fine tune the filtering, reducing artifacts at a cost of decreasing the sharpness of the frequency rejection. The x-axis scale of the power spectrum may be changed with the Max Displayed Period slider to look at long or short periods. All slider controls may be incremented or decremented by one-second intervals by clicking on the arrow controls. Numerical values may also be entered directly into the control display boxes.

The thin film filter and photoresist filter are bandpass filters, and their use is straightforward. One caution to keep in mind is that any waveform containing white noise has spectral components at all frequencies. Thus, by selecting a very narrow region in any part of the spectrum, a bandpass filter will always yield a smooth, sinusoidal waveform, which is nothing more than an artifact. Thus, bandpass filters should always be used to isolate significant features in the power spectrum.

The interface detector uses a second derivative to enhance discontinuities in slope that occur at interfaces. The bandpass settings must be as follows: Set the Long cutoff to a value below the most significant peaks in the power spectrum in order to reject derivative oscillations from both thin films and photoresist. Set the Short cutoff to reject noise. The extent has a significant effect with this filter. An extent of 2 would result in a finite-difference approximation to the derivative that would give an accurate second derivative on noise-free data. However, this extent is not sufficient to bandpass filter thin film oscillations, so an extent that effectively covers a period of the thin film oscillations serves to suppress oscillatory terms. Unfortunately, a larger extent also leads to "ringing" oscillations near kinks. These artifacts distort the shape of the true derivative. Experimentation with the filter settings will yield some spike-like behavior near interfaces that can be used for interface identification, but no hard-and-fast rules can be made about the direction or shape of the derivative spikes.

Digital filter methods

It is straightforward to filter the reflectance waveform using digital filtering methods. However, there is a conflict between the desire of the etching tool operator to be provided with a real-time update of the most recent filtered data value and the intrinsic limitations of the uncertainty principle. In its most basic form, the uncertainty principle demands that a given frequency can be filtered out only after a minimum of roughly one wavelength period of time has elapsed. Two digital filtering approaches have been put into Monoetch that spread the uncertainty consequences into different parts of the waveform.

The FIR filter

The Finite-Impulse Response (FIR) filter is a moving window that convolutes the input waveform with $2m$ coefficients using data that extends $\pm m$ points to either side of the resulting filtered point:

$$\bar{y}_i = \sum_{k=-m}^{m} c_k y_{i+k}$$

Because the filter extends $\pm m$ points to either side of the input, the most recent data at $i+m$ will not have a filtered output value until another m data points have been collected. It is possible to shift the window to avoid this situation, but this simply places a phase lag in the filtered output identical to the time it takes to obtain m additional points.

When the FIR filter is used as a bandpass device, the sharpness of the cutoffs are proportional to the number of terms used in the data window and a function of how far the data window extends in real time. In Monoetch applications, for example, it is unreasonable to assume that photoresist oscillations with a period of 150s can be separated from film oscillations having a period of 20s using a filter that spans only 1s.

The disadvantage of the FIR window "blankout" effects at each end of the waveform is compensated by the fact that a filtered value, y_i, once determined, will not change. This is not the case for FFT filtering.

The FFT filter

The Fast Fourier Transform (FFT) method of filtering is often used for post-analysis of data waveforms. A frequency spectrum of the time-dependent waveform is obtained using the FFT. Selected ranges of the frequency spectrum are set to zero, and the modified spectrum is reverse-transformed back to a filtered waveform. The resulting waveform has values over the complete time range of the data,.unlike the FIR filtered waveform, but the ends of the data are nonetheless distorted with "Gibbs oscillations" caused by the truncating effects of the filtering in the frequency domain. These artifacts may be reduced by "windowing the data", with a triangle function or smoother transition, at a cost of sharpness in the cutoff. Because the FFT is a batch operation, the appearance of the filtered waveform will change as more data is added to the raw array.

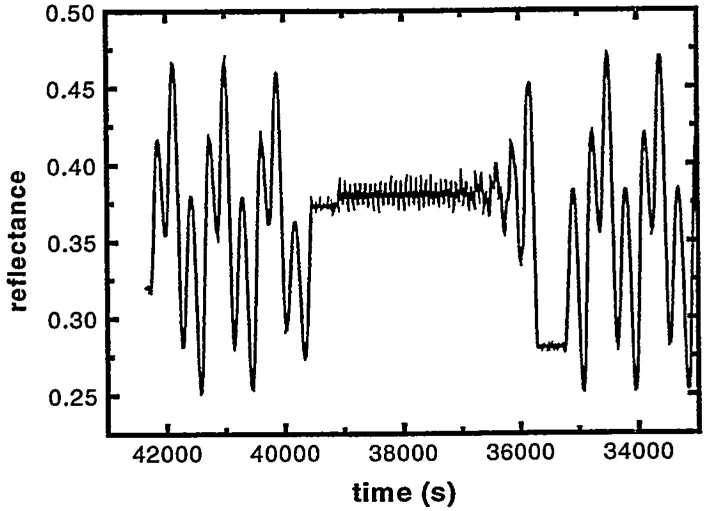

Fig 6: Reflectance spectrum taken during the MBE growth of a reflectance modulator structure

Example of digital filtering

The following gives a brief example of the effects of FIR filtering on the reflectance waveform of a patterned reflectance modulator device structure. Fig 6 shows the time-reversed reflectance plot of the last part of a device structure grown by MBE. The reflectance shows a top mirror-stack structure followed by an active region with 38 very thin layers, followed by another mirror stack. Fig 7 shows the raw reflectance signal at the same wavelength taken during ICP etching of a patterned sample.

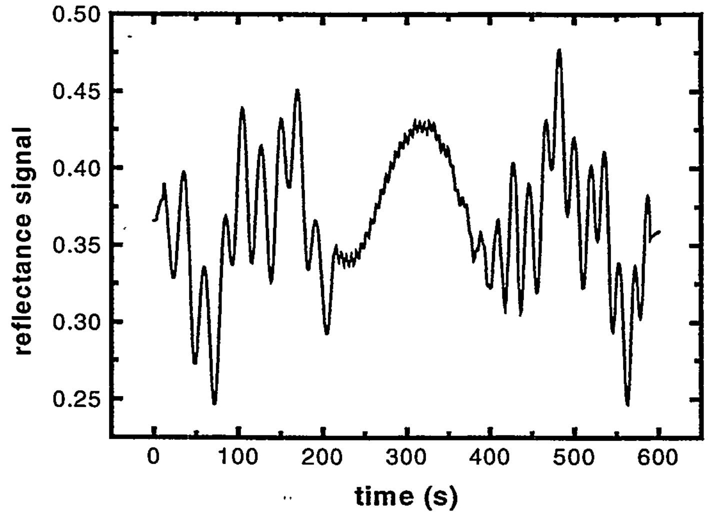

Fig 7: Reflectance waveform of the reflectance modulator grown in Fig. 5 during the ICP etching of a patterned sample.

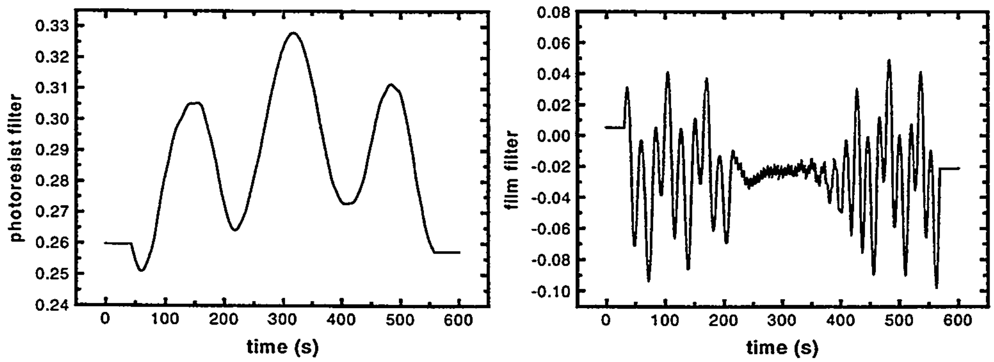

Fig 8: Filtered waveforms from Fig 7. Photoresist oscillations are seen with a lowpass filter. Thin film oscillations are seen with a bandpass filter that excludes the photoresist oscillations. Note the "blankout" regions at each end of the waveform. The extent of the FIR filter window does not allow a filtered value to be calculated in these regions.

The same reflectance features are exhibited in both waveforms, but the slow photoresist oscillations make it difficult to identify detailed layers and interface positions. Fig. 8 shows the results of photoresist and film oscillation bandpass filtering on the raw etching reflectance profile. The lowpass filter (short = 111s, long = 500s, extent = 77) shows three slow oscillations due to photoresist. The bandpass filter (short = 5.1s, long = 92s, extent = 56) brings out many of the features seen in Fig 6 due exclusively to thin-film oscillations.

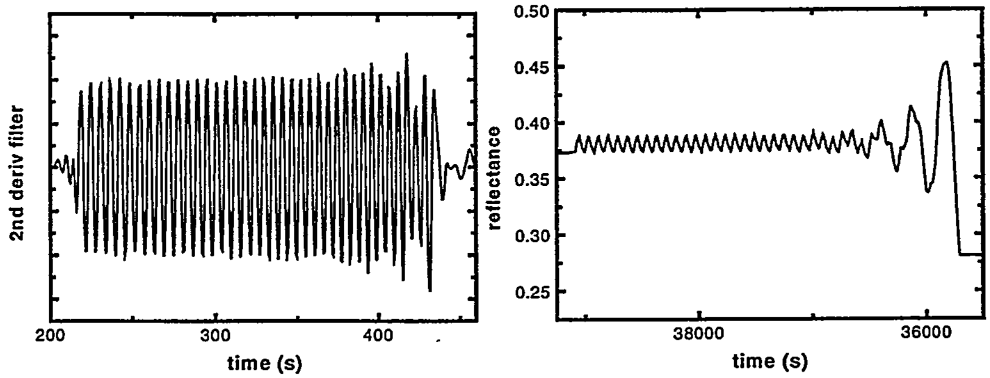

Fig 9: Second-derivative bandpass filtering in the active region (left trace) compared to the reflectance waveform from the MBE growth run in Fig 6. The second derivative bandpass filter ignores photoresist and thin film oscillations and enhances discontinuities in the slope.

Fig. 9 compares the second-derivative bandpass Interface Detector filter (short = 4s, long = 8.5s, extent = 30) applied to the active region of the structure. The second derivative creates spikes at sharp interfaces. 38 downward spikes mark the positions of the 38 layers seen in the original growth reflectance spectrum.

Hardware connections

Monoetch 2.0 currently supports three methods for inputting reflectance signals. Two A/D multifunction boards from National Instruments http://www.natinst.com are supported: the AT-MIO16-X is a 16-bit multifunction board for an ISA slot. The DAQCard™ AI-16XE-50 is a 16-bit multifunction PCMCIA card for laptop computers. Monoetch uses only channel 0 (and optionally, channel 1) of the A/D converter functions of either of these boards. However, the digital I/O may be used for future remote control applications, and the timing features will be used in future data gathering operations. The third hardware option is the Stanford Research (http://www.srsys.com) SR810 lock-in amplifier for data collection schemes requiring chopped light. Monoetch communicates with this instrument through serial port COM1 or COM2. The hardware used in a given application is specified in the .cfg file (see *Hardwired variables*) as a "Data Gathering Unit" (DGU).

The .cfg file

The first action taken by Monoetch is to read in a configuration file that has customized data collection settings stored so that the GUI can be reset to these values whenever the program is re-started. The configuration file is identified by a ".cfg" extension and must be stored in the same folder as the Monoetch executable. Monoetch allows multiple configurations to be stored in the same folder. If more than one .cfg file is found, Monoetch opens up a file dialog box to allow the user to select a particular .cfg file. If only one .cfg file exists, it is read directly.

The .cfg file is an ASCII text file, readable and editable with Notepad or other text editor. Configuration values are given as the first word of a line, followed by a text comment to help a user locate a particular value for editing. Typically, however, the .cfg file is never changed this way because it is easier to use the Save Settings command within Monoetch. If a text editor is used to change the .cfg file, care must be taken to not change the order or number of arguments on each line. Below is a listing of a typical .cfg file.

```
#monoetch startup values. Do not change order.
2.0     Version Number
ATMIO16X    Data gathering unit, DGU (ATMIO16X,SR810, DAQCardAI16XE50, SIMULATION)
1       Unit value (A/D Board ID, COM Port)
1.0e-4      Time base for sample interval measurement (1e-4 or 1e-3)
# The following are saved with Save Settings command in Monoetch
0.050       DGUtimer interval (0.03, 0.05, 0.10, 0.3)
100     Number of points in the stripchart plot (50,100,200)
1       gain (DGU specific, but must be 1 <= gain <= 100)
1       Polarity (1 is positive, 0 is negative)
550.5       wavelength (nm)
0.50        Sample Period (0.3,0.5,0.75,1.0)
1.53        Endpoint Factor
0       Filter method (0 FFT, 1 FIR)
1       Cursor Mode (0 Lasso, 1 Hot)
#Digital filter cutoffs pshort, plong, extent, for kink, films, and photoresist,
respectively
4.538889    15.700000   100
7.261111    124.689796  0
111.888889  206.144444  9
```

A more detailed description of the variables used in the .cfg file follows.

Hardwired variables

The following variables are used by Monoetch, but have no GUI controls to alter their values. They may be changed only by editing the .cfg file with an ASCII text editor such as Notepad.

`monoversion:`	This is used to compare the version number stored in the .cfg file with the version number of Monoetch.
`DGU:`	String defining the hardware data gathering unit. Current possibilities are ATMIO16X, DAQCardAI16XE50, SR810, and SIMULATOR. The SIMULATOR option is useful for an office

Monoetch application with a computer that has no signal gathering equipment.

`DGUval`:	Device-dependent code. For ATMIO16X and DAQCardAI16XE50, it is the board number assigned in the NIDAQ configuration utility. For SR810 it is the serial COM port number used to query the lock-in.
`timebase`:	Monoetch stores its data in a compressed format labeled a "time-stamped binary" (.tsb) file (see Data file format). In this format, the time interval between data points is stored as an unsigned 16-bit integer that is equal to the number of timebase units in the time interval. Typical values for the timebase are 10^{-4} s or 10^{-3} s, allowing a maximum of 6.5536 s or 65.536 s, respectively, between data points.

GUI-based variables

The following variables are used by Monoetch and have GUI controls or menu options for changing their values.

`DGUinterval`:	Time interval, in seconds, between DGU acquisitions. Typically 0.05
`stripBufSize`:	The Latest Data display in Monoetch is a stripchart record of the most recent data taken during the run. The number of data points in the display is given by `stripBufSize` with the following possible values: 50, 100 and 200.
`gain`:	Gain setting or sensitivity setting for the A/D board or lock-in, respectively. This is device-dependent.
`polarity`:	Describes the signal polarity as either positive or negative.
`lambda`:	Wavelength, in nm, of the light used to collect reflectance. This value is stored in the header of the data file.
`DisplayTime`:	Time interval, in seconds, between data display events.
`Efactor`:	Endpoint factor for endpoint prediction. See Endpoint Prediction for a description.
`FilterMethod`:	If 1 then FIR filtering is used. Otherwise FFT filtering is used. See **Digital filter methods** for a description of these methods.

`CursorMode.`	If 1, then the main graph display is "Hot", allowing endpoint markers to be set by clicking in the display. If 0, then the display is in "Lasso" mode. Dragging the cursor over the main graph display creates a zoomed display of the dragged rectangle with cursors available for setting markers.

Data file format

Monoetch stores the reflectance waveform in a compressed format called "time-stamped binary". The files are given an extension: ".tsb". These are binary files that are designed to efficiently store reflectance data having unevenly-spaced time intervals. Each reflectance value is stamped with a time value. Time resolution is maintained by recording time intervals, rather than total elapsed time, in units of 10^{-4} seconds. The reflectance is stored as a signed 16-bit integer that maps normalized raw reflectance signals ranging from 0 to 1 (corresponding to zero to full scale) as the integer 0 to 65535.

The .tsb file consists of a 16 byte header that defines the scaling for wavelength and time:

- nw: 2-byte, 16bit signed integer giving the number of spectral wavelength values in the file. Monoetch data files always set nw to 1.
- nt: 2-byte, 16bit unsigned integer giving the number of time values in the file. This places a maximum of 65535 time values that can be stored.
- wzero: 4-byte float giving the wavelength of the first spectral value. Monoetch places the wavelength in this position.
- wdelta: 4-byte float giving the slope of the wavelength scale. wavelength[i] = wzero + i * wdelta. Monoetch sets this value to zero.
- tUnit: 4-byte float giving the time unit for intervals between data points. The time data is stored as a 2-byte 16bit unsigned integer giving the number of time units that elapsed between the current and previous spectrum (interval = (unsigned int value) * tUnit). Typical values for tUnit are 10^{-3} (maximum of 65s between data points) or 10^{-4} (maximum of 6.5s between data points). Monoetch uses the highest time-resolution value consistent with the sample period. Total elapsed time for a waveform is calculated as a running sum over each time interval.

The header is followed by a continuous block of 2-byte integers representing the time and reflectance data. The order of storage is the time interval value followed by reflectance value. This is repeated nt times, yielding nt * 2 total integers.

Format conversion

A GUI-based utility, Convert, is available to convert .tsb files to ASCII files that can be read by plotting and spreadsheet applications. Each time and reflectance pair are placed on a line, separated by a space. No header information is provided. The converted file is given the extension .dat.

Appendix C

Spatially-Resolved Ion Trajectory Measurements During Cl_2 Reactive Ion Beam Etching and Ar Ion Beam Etching

To be published in Journal of Vacuum Science and Technology

Presented as an invited paper at the 43rd International Conference on Electron, Ion, and
Photon Beam Technology & Nanofabrication
Marco Island, FL, USA, June 1-4, 1999

Spatially-Resolved Ion Trajectory Measurements During Cl_2 Reactive Ion Beam Etching and Ar Ion Beam Etching *(invited paper)*

G. Allen Vawter, Joseph R. Woodworth and Walter J. Zubrzycki
Sandia National Laboratories, P.O. Box 5800, Albuquerque, NM 87185-0603

ABSTRACT: The angle of ion incidence at the etched wafer location during RIBE and IBE using Cl_2, Ar, and O_2 ion beams has been characterized using an ion energy and angle analyzer. Effects of beam current and accelerator grid bias on beam divergence and the spatial uniformity of the spread of incident angles are measured. It is observed that increased total beam current can lead to reduced current density at the sample stage due to enhanced beam divergence at high currents. Results are related to preferred etch system design for uniform high-aspect-ratio etching across semiconductor wafers.

INTRODUCTION

Control of etched sidewalls created during reactive-ion-beam etching (RIBE) of compound semiconductors is an area of intense interest within the integrated optics community. Optical circuits such as integrated etched-facet diode lasers and photodetectors, optical waveguide bends using total-internal-reflection mirrors, and tilted or curved laser diode output coupling facets all require extremely smooth facets with facet angle control within one or two degrees. It is generally accepted that the angular divergence within a Cl_2 ion beam plays a significant role in the evolution of etched sidewalls. This has been supported by numerical models[1] and limited experiments[2] where sidewall angle as a function of etch system configuration has been measured. However, until now, direct measurements of ion beam flux angular distribution along a cross section through the beam have not been performed.

The vast majority of published work discussing side-wall angles in RIBE has been done with small ion sources at large source-to-sample distances [3] in order to minimize the effects of beam spread on the etched profile. However, such long-working-distance configurations with a small ion source provide little control the incident ion angle, lead to poor uniformity of incident angle across the etched substrate, and do not scale up to large wafer processes[4]. Use of a larger ion source gives more uniform etch rates over reasonable wafer sizes but little is known about the uniformity of the etched facet angles. Since facet angle and shape are intimately related to the incident ion angle, a direct measurement of incident ion angle would be very useful in determining an optimized etch configuration. We report the first ion beam flux trajectory measurements in a broad-area dual grid RIBE system with an inductively-coupled plasma (ICP) source. In addition to spatial variation of the total ion flux across the beam diameter, (the conventional measure of ion beam uniformity) the distribution of incident ion angle is measured as a function of position along the beam diameter. Data is collected for Cl_2, O_2, and Ar ion beams as a function of grid bias and beam current using a specially constructed ion energy and angle analyzer[5] positioned on a linear translation stage located at the standard position of the etch piece in our RIBE system.

EXPERIMENT

The etch system (Fig. 1) was custom built with ultra-high vacuum capability for non-selective etching of GaAs and AlGaAs using a Cl_2 ion beam. The ion source is an ICP-type excited by a 13.5 MHz RF power supply with 15 cm diameter dual pyrolytic graphite grids. The voltage on the screen grid, nearest to the ICP plasma, controls the ion beam energy. The voltage on the accelerator grid, nearest to the sample stage, controls the angular divergence of the ion beam exiting the source. The grids have a uniform array of 1.2-mm-diameter holes in a hexagonal pattern on 4 mm centers. The working distance between the grid and sample stage is 35 cm giving a maximum line-of-sight angle from the center of the stage to the edge of the grid of 12° and an 18° maximum angle at the edge. Barring curved ion trajectories, these are the maximum angles from normal incidence at which an ion may impact the etched sample at the middle and edge of the stage. A beam neutralizer is located downstream from the grids to provide a source of electrons which move along with the beam to minimize space charge effects and charge build-up in the etch piece. The etch piece is located on a 75-mm-diameter Mo block capable of water or liquid-nitrogen cooling and of resistive heating which provides an operating range of –50° C up to 400° C. A thermocouple is embedded in the back surface of the Mo block to measure the sample temperature. Finally, the entire Mo block and heater assembly is passed out through a load lock, using a magnetic-coupled transfer arm, for loading and unloading of etch pieces.

The etch reactor was modified for the purposes of this experiment by the replacement of the sample stage with a custom built ion energy and angle analyzer located at the same distance from the ion source. The analyzer (Fig. 2) comprises a Faraday-cup-type ion current detector with circular concentric detection electrodes located under a pin hole aperture and may be moved laterally along the beam diameter to measure spatial variations in angle-resolved ion flux. Differential pumping of the Faraday cup behind the pinhole minimizes scattering of ions within the analyzer. The concentric electrodes effectively "bin" ion current into components within specific angle-of-incidence ranges. These are centered on mean angles of 1.7°, 4.2°, 6.9°, 9.1°, 12°, 14.4°, 16.8°, 19.5°, and 27.5° from surface normal of the sample stage. Finally, the analyzer is equipped with a repeller screen, typically biased at –80 V, to prevent electrons from impacting the electrodes and canceling a portion of the positively-charged ion current. As an experimental note, variation of the voltage on the "analyzer grid" permitted direct measurement of the energy spread within the ion beam. This energy spread was found to be 20-30 eV for most of the beams described below, although the oxygen ion beam energy spread was 100 eV.

Several ion beams were characterized using the analyzer. These beam conditions correspond to etch setups routinely used in our laboratory during compound semiconductor device fabrication. These are: 1) an Ar ion mill at 400 eV, 120 mA beam current, 0.25 mTorr pressure, and -200 V accelerator bias; 2) Cl_2 RIBE at 350 eV, 70 mA, 0.25 mTorr, -270 V accelerator bias; 3) Cl_2 RIBE at 400 eV, 40 mA, 0.25 mTorr, -480 V accelerator bias; 4) Cl_2+Ar RIBE at 400 eV, 120 mA, 0.275 mTorr, -100 V accelerator bias; 5) O_2 RIBE at 400 eV, 100 mA, 0.78 mTorr, -25 V accelerator bias. Ion beam (1) is an Ar ion mill typically used for removal metal films from semiconductor substrates and devices. Beams (2) and (3) are reactive ion beams used for highly anisotropic etching of AlGaAs.[6] Beam (4) is a Cl_2 and Ar mixed beam (53% Cl_2) used for etching rib optical waveguides in AlGaAs. Beam (5) is an O_2 ion beam used for etching photoresist.

RESULTS AND DISCUSSION

Spatial Uniformity

Data for spatially resolved ion flux are shown in Figures 3 through 7. Looking at just the narrow angle components below 4.2°, a wide uniform region of ~7.5 cm is evident for all etch conditions. Larger-angle components are less uniform. All data except O_2 show a dip in ion flux at the center of the beam for angles greater than or equal to 14.4°. This dip at high angle is understood with the help of Figure 1 where it is seen that ions from the edge of the grid have a line-of-site elevation of 12° from normal. Moving the analyzer off of beam center introduces higher angle ion-current components from the far side of the grid.

These purely geometric considerations explain most of the characteristics of the spatial data. Clearly, in situations where only very "near-normal" ion impacts are desired a system with large grid-to-sample spacing and a grid diameter equal to the sample diameter may function best. This will take advantage of the uniformity of the low-angle ion current while preventing the bulk of the high-angle ion current from impacting the etch sample. However, such a configuration will not scale well to large wafer sizes since increasing the grid and wafer diameter will eventually cause significant high-angle ion current to reach the edge of the wafer causing non-uniform etch profiles.

Etch applications needing significant off-normal ion impacts for efficient side-wall cleaning and wall angle control will benefit from a moderate grid-to-sample spacing and a large-diameter grid such that ions at the outer envelope of the beam divergence will impact the center of the sample. For example, increasing the diameter of our 15 cm grid would reduce the dip in the high-angle current at the beam center (see Fig. (4), 14.4° band). It would also be possible to reduce the dip by increasing the grid-to-sample distance. However, this has the effect of reducing the high-angle current at the wafer edges rather than increasing the high-angle current at the center of the wafer. The spatially-resolved data is strong verification that the maximum ion incident angles desired are related to the grid working distance and grid diameter. However, it is also clear that simple geometric methods assuming straight ion trajectories from each grid hole are adequate for first-order approximations of ion-beam angular uniformity.

Accelerator bias

The accelerator grid bias data shows quite clearly the influence of this grid on the beam quality. The effects of varying accelerator grid bias at fixed beam current and energy are shown in Figures 8 through 11. A key similarity of all data is the characteristic peak of ion current at low angles where beam divergence is at a minimum. Deviation of the accelerator bias above or below this optimal value will increase the beam divergence.

Accelerator grid influence on a 400 eV·Cl_2 low current beam of only 40 mA is shown in Figure 8. At this low beam current very little accelerator bias is needed to pinch the beam to its smallest divergence. The minimum divergence is seen at 50 to 60 Volts with an abrupt spreading of the beam beyond 60 Volts. Compare this to Figure 9 showing accelerator grid influence on a higher-current Cl_2 beam of only slightly lower energy but with the beam current nearly doubled to 70 mA. A broad region of narrow divergence is seen and the accelerator bias for minimum divergence has moved out to between 100 and 120 V. The mixed Cl_2 + Ar beam (Fig. 10) at 400 eV, 120 mA, shows that a still higher accelerator bias is needed for minimum beam divergence with a relatively mild enhancement of beam divergence at accelerator bias values on either side of the 220 V optimum. The characteristic of O_2 is shown in Figure 11. This is a high current,120 mA, beam at a relatively high pressure of 0.78 mT. Again a broad region of narrow divergence is seen with an optimal point near 120 V.

Both Figures 10 and 11 show a sudden increase in low-angle current at very low accelerator bias: In the case of the Cl_2+Ar beam, the current drawn by the accelerator grid during data collection was observed to increase from 2.4 mA to 17.7 mA as the accelerator bias was changed from -150 to -50 V. However the accelerator current abruptly dropped to 0.3 mA at -6 V, the bias value corresponding to the sudden jump in low-angle current. Similar, but less extreme, behavior was observed in the case of the O_2 beam. The drop in measured accelerator grid current is symptomatic of poor rejection of backstreaming electrons at low accelerator grid bias.[4] At such low accelerator bias potentials electrons from the neutralizer may actually impact the accelerator grid. The negatively-charged electron flux would cancel a portion of the positively-charged ion flux hitting the grid resulting in a reduced net current flow through the grid. Backstreaming electrons may also be pulled into the screen grid where they can alter the beam formation process and influence the divergence of the beamlet emerging from each hole in the grid set.

Beam Current Variation

With one exception, divergence data as a function of beam current was taken at a fixed neutralizer current of 120 mA. This decision was made in consideration of the ion source manufacturer's recommendation that the filamentless bridge neutralizer (FBN) not be operated below 100 mA discharge current. In one case, Cl_2 at 350 eV, the neutralizer was matched to the beam current over the range of tested currents. The limited time available to perform the wide range of experiments discussed in this paper prevented a careful analysis of neutralized and unneutralized ion beams.

Data for ion beam divergence as a function of beam current are shown in Figures 12 through 15. In all cases, as the beam current is raised from approximately 25 mA the shape of the beam is unchanged up to a critical current between 80 and 100 mA. The general conclusion is that an optimal total beam current exists for minimum beam divergence. In all cases, ion beam currents in the range of 80 to 125 mA are seen to provide the lowest beam divergence. Beyond this current, the ratio of low-angle (1.7 and 4.2°) to high-angle current drops as the ion beam spreads. It is also observed that, as beam current is increased beyond that of the peak in the low-angle current, the total current measured by the analyzer drops. (The total current is obtained by summing all of the individual current components and is not shown in the figures.) This phenomena reflects an actual drop in beam-current density at the center of the ion beam and is a direct result of the etch geometry. Referring to Figure 1, it can be seen that 12° is the largest angle representing line-of-sight from the analyzer located at the center of the beam to a grid hole at the edge of the grid set. (In the figures, some ion current is observed in the 14.4° band and the signal level in the 16.8° and higher bands is very low or zero. The presence of current measured at 14.4° is felt to be due to stray fields within the analyzer or possibly some curvature of the ion path after leaving the grid set.) At large ion beam currents the divergence of the beam is sufficient to reduce the current density at center of the etched wafer. For example, at ion currents greater than 150 mA in Figure 12, a significant portion of the ion current may be at angles greater than 12° such that even ions from the edge of the grid set are spread out with some ions passing through the middle of the beam prior to impacting the wafer. Referring back to the uniformity scans of Figures 3-7, this situation may be visualized as adjusting the ion beam parameters to an extreme wherein even the low-angle current contributions show two local maxima symmetric about, but removed from, the beam center. Thus it is seen that, in our configuration of fixed neutralization current under the given grid and stage geometry, increasing the ion beam total current does not monotonically increase the ion current density at the stage center. A clear maximum current density is achieved at a particular total beam current. Increasing the ion beam current beyond this value actually spreads the ion beam and decreases the ion current density at the center of the etched wafer.

The situation of a fully neutralized ion beam, Figure 14, is only slightly different from that of the fixed neutralization current. Matching the neutralization current to the ion beam current pushes the peak current for lowest divergence out to approximately 125 mA compared with 80 to 100 mA for the fixed neutralizer. The fully neutralized beam also has a clearly reduced divergence, compared to incomplete neutralization, at the maximum-tested current of 200 mA.

SUMMARY

Using a specially-configured ion energy and angle analyzer installed in a large-area RIBE system, the local ion angle and trajectory within the ion beam at the location of the etched wafer has been measured. The uniformity of the ion beam current along a diameter of the beam shows a clear angular dependence derived directly from the choice of grid diameter and working distance. Low-angle ions tend to be spatially uniform in distribution while high-angle ion current density peaks away from the center of the wafer. Selection of the accelerator grid bias has a strong influence of ion beam divergence with minimum divergence occurring for accelerator biases of between –50 V and –200 V. Of particular interest is the observation that ion current density at the center of the wafer is not monotonically related to the choice of ion beam current. A clear optimal total beam current exist for which the current density is a maximum. Increasing the beam current beyond this value serves only to increase the beam divergence and actually decrease the current density at the center of the wafer.

The impact of this study on high-aspect-ratio etching can be clearly seen during examination of Figs 8 through 11 for accelerator bias and Figs 12 through 15 for ion beam current. At a given ion energy and pressure, the accelerator bias and beam current selection play an important role in beam divergence and the resulting etched profile. Both need to be optimized for the application. Once the desired etched profile is achieved, the beam current cannot be adjusted up or down without changing the etched profile.

Sandia is a multiprogram laboratory operated by Sandia Corporation, a Lockheed Martin Company, for the United States Department of Energy under Contract DE-AC04-94AL85000.

REFERENCES

[1] M. Hagberg, B. Jonsson and A. G. Larsson, J. Vac. Sci. Tech. B**12**(2), 555-66 (1994).

[2] W. J. Grande, J. E. Johnson and C. L. Tang, J. Vac. Sci. Tech. B**8**(5), 1075-9 (1990).

[3] G. A. Lincoln, M. W. Geis, S. Pang N. N. Efremow, J. Vac. Sci. Tech. B**1**(4), 1043-6 (1983).

[4] T. Jolly, *Handbook of Ion Sources* , Ed: B. Wolf, (CRC Press, 1995), pp. 209-237.

[5] J. R. Woodworth, M. E. Riley, P. A. Miller, G. A. Hebner and T. W. Hamilton, J. Appl. Phys. **81**(9), 5950-5959 (1997).

[6] W. J. Zubrzycki, G. A. Vawter and J. R. Wendt, J. Vac. Sci. Tech. (To be published, same issue as this article.) (1999).

FIGURE CAPTIONS

Figure 1: Schematic of the RIBE system. Layout lines are included for grid working distance and angles from perimeter of grid to center and edge of sample stage.

Figure 2: Schematic of the ion trajectory analyzer. During this experiment, the beam entrance aperture was placed in the plane of the sample stage. The sample stage was removed.

Figure 3: Angle-resolved uniformity of ion flux for Ar IBE under conditions shown in the figure.

Figure 4: Angle-resolved uniformity of ion flux for low-current Cl_2 RIBE under conditions shown in the figure.

Figure 5: Angle-resolved uniformity of ion flux for moderate-current Cl_2 RIBE under conditions shown in the figure.

Figure 6: Angle-resolved uniformity of ion flux for high-current mixed Cl_2 + Ar RIBE under conditions shown in the figure.

Figure 7: Angle-resolved uniformity of ion flux for high-current O_2 RIBE under conditions shown in the figure.

Figure 8: Angle-resolved ion flux versus accelerator grid bias for low-current Cl_2 RIBE under conditions shown in the figure.

Figure 9: Angle-resolved ion flux versus accelerator grid bias for moderate-current Cl_2 RIBE under conditions shown in the figure.

Figure 10: Angle-resolved ion flux versus accelerator grid bias for high-current mixed Cl_2 + Ar RIBE under conditions shown in the figure.

Figure 11: Angle-resolved ion flux versus accelerator grid bias for high-current O_2 RIBE under conditions shown in the figure.

Figure 12: Angle-resolved ion flux versus ion beam current for Ar IBE under conditions shown in the figure.

Figure 13: Angle-resolved ion flux versus ion beam current for mixed Cl_2 + Ar RIBE under conditions shown in the figure.

Figure 14: Angle-resolved ion flux versus ion beam current for Cl_2 RIBE under conditions shown in the figure. The neutralizer current is matched to the ion beam current.

Figure 15: Angle-resolved ion flux versus ion beam current for O_2 RIBE under conditions shown in the figure.

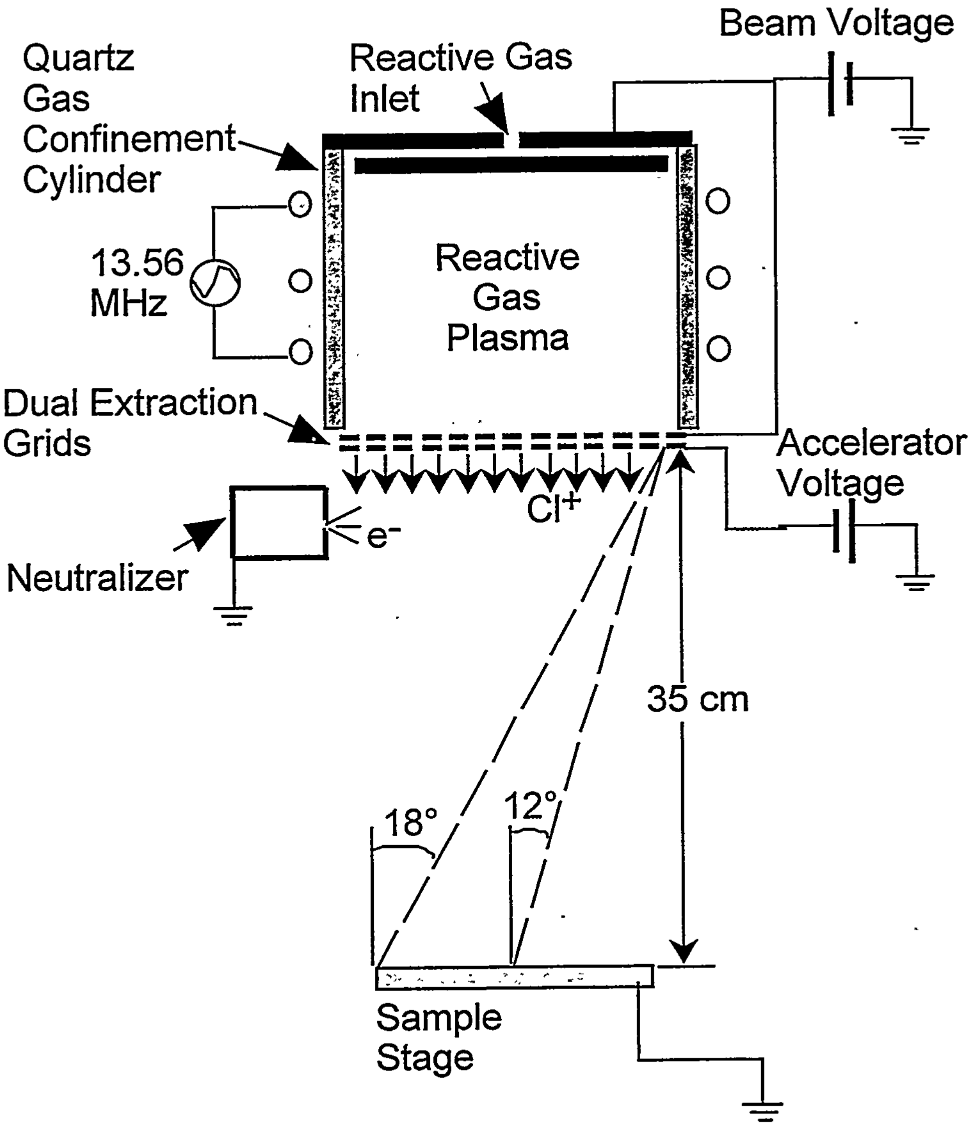
Beam Voltage
Quartz
Gas
Confinement
Cylinder
Reactive Gas
Inlet
13.56
MHz
Reactive
Gas
Plasma
Dual Extraction
Grids
Accelerator
Voltage
Cl+
e-
Neutralizer
35 cm
18°
12°
Sample
Stage

Fig 1

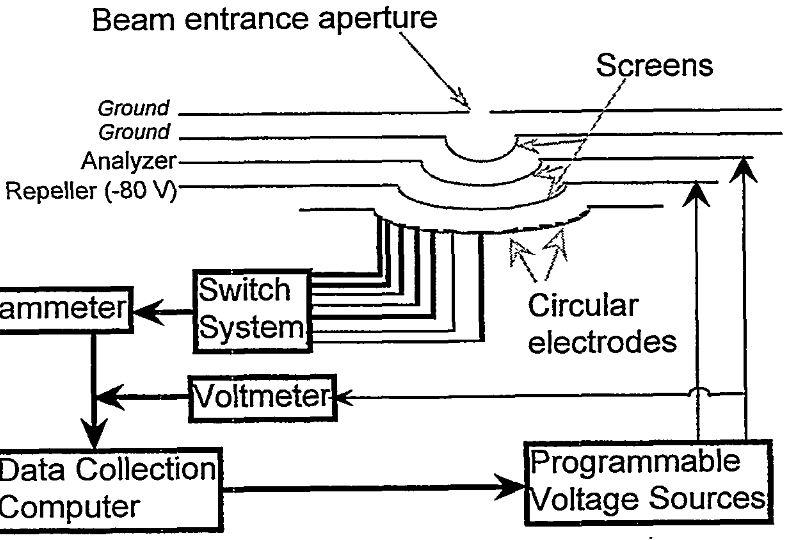
Beam entrance aperture
Screens
Ground
Ground
Analyzer
Repeller (-80 V)
Circular electrodes
picoammeter
Switch System
Voltmeter
Data Collection Computer
Programmable Voltage Sources

Fig. 2

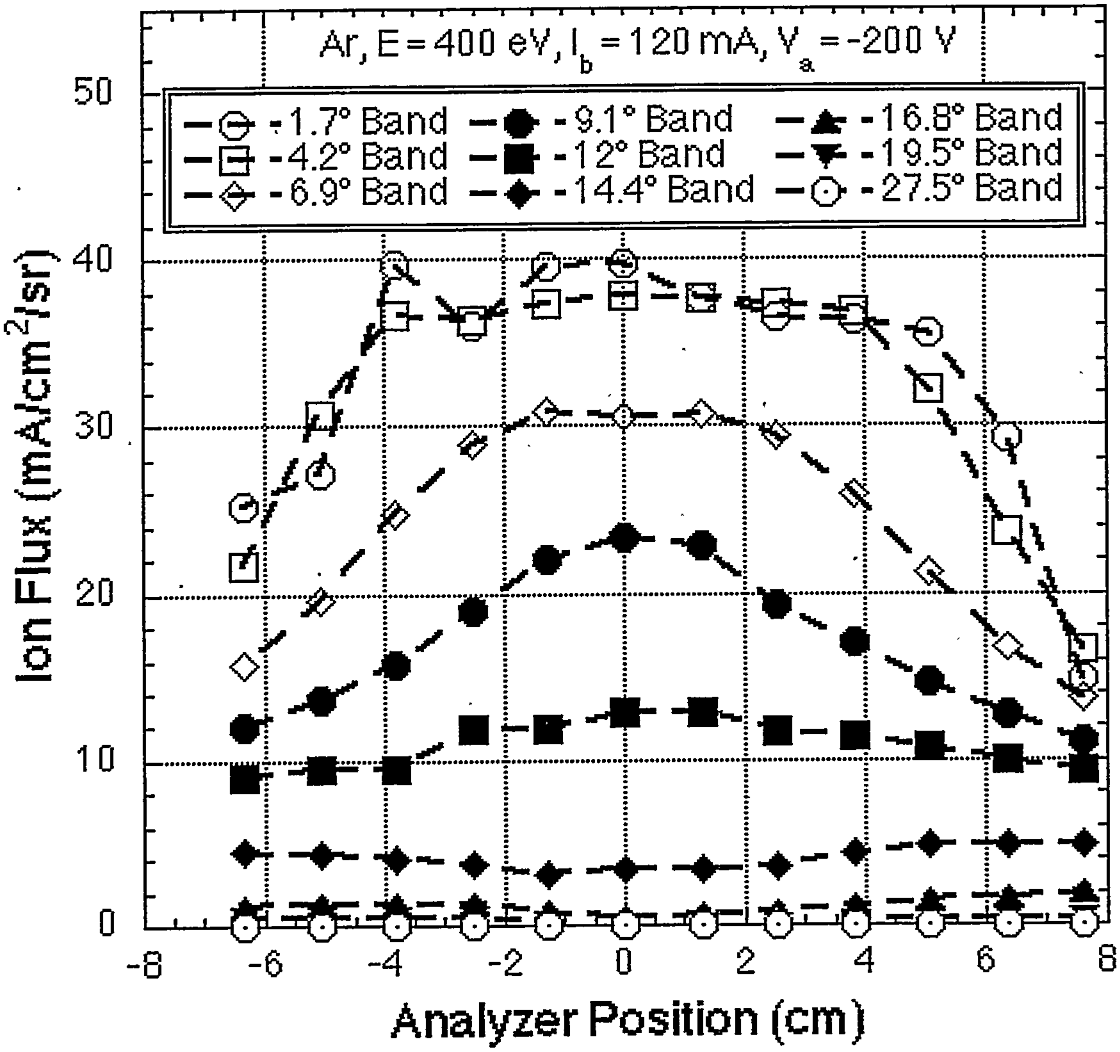
Ar, E=400 eV, I_b=120 mA, V_a=-200 V
1.7° Band
4.2° Band
6.9° Band
9.1° Band
12° Band
14.4° Band
16.8° Band
19.5° Band
27.5° Band
Ion Flux (mA/cm^2/sr)
0
10
20
30
40
50
-8
-6
-4
-2
0
2
4
6
8
Analyzer Position (cm)

Fig. 3

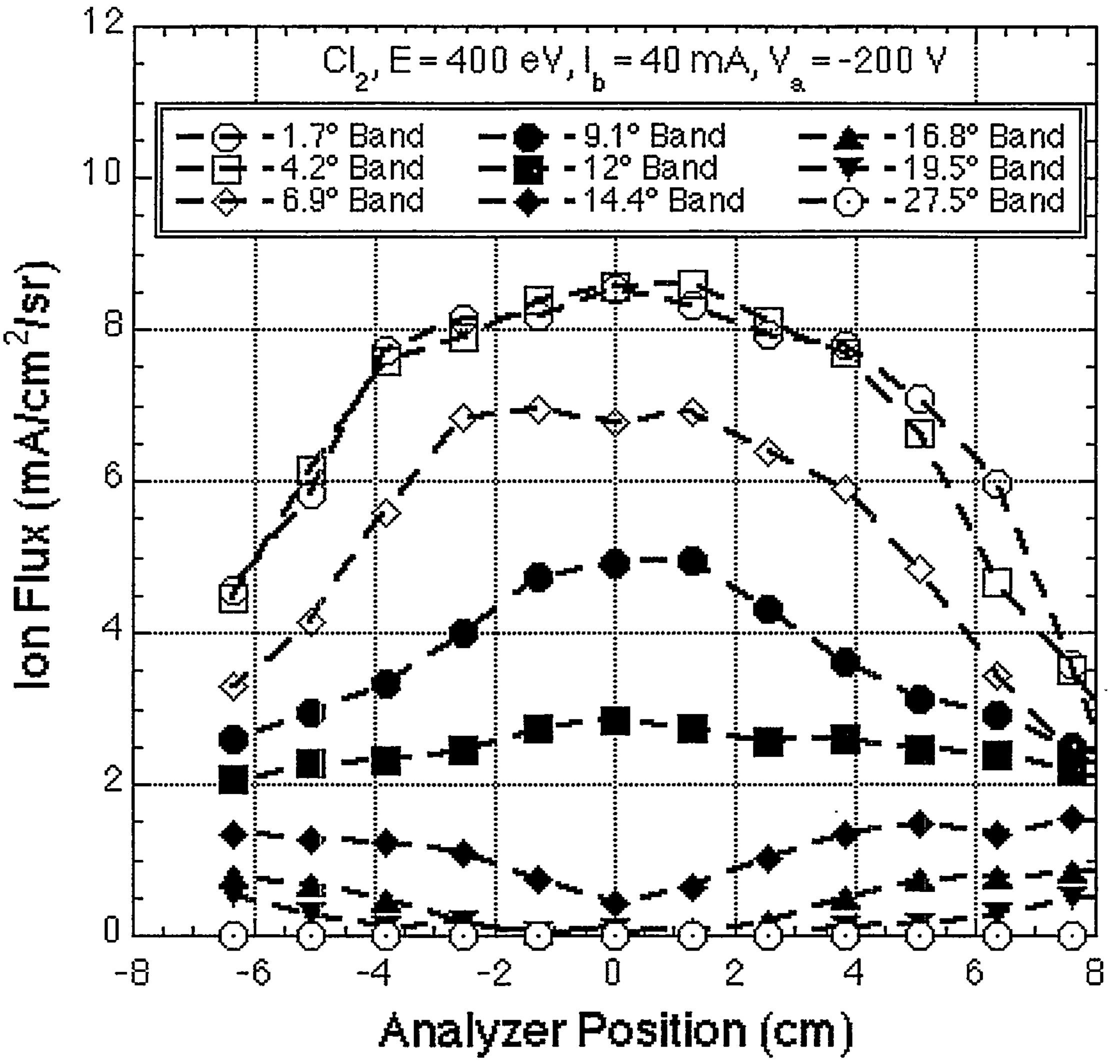

Cl_2, E = 400 eV, I_b = 40 mA, V_a = -200 V
1.7° Band
4.2° Band
6.9° Band
9.1° Band
12° Band
14.4° Band
16.8° Band
19.5° Band
27.5° Band
Ion Flux (mA/cm^2/sr)
0
2
4
6
8
10
12
-8
-6
-4
-2
0
2
4
6
8
Analyzer Position (cm)

Fig. 4

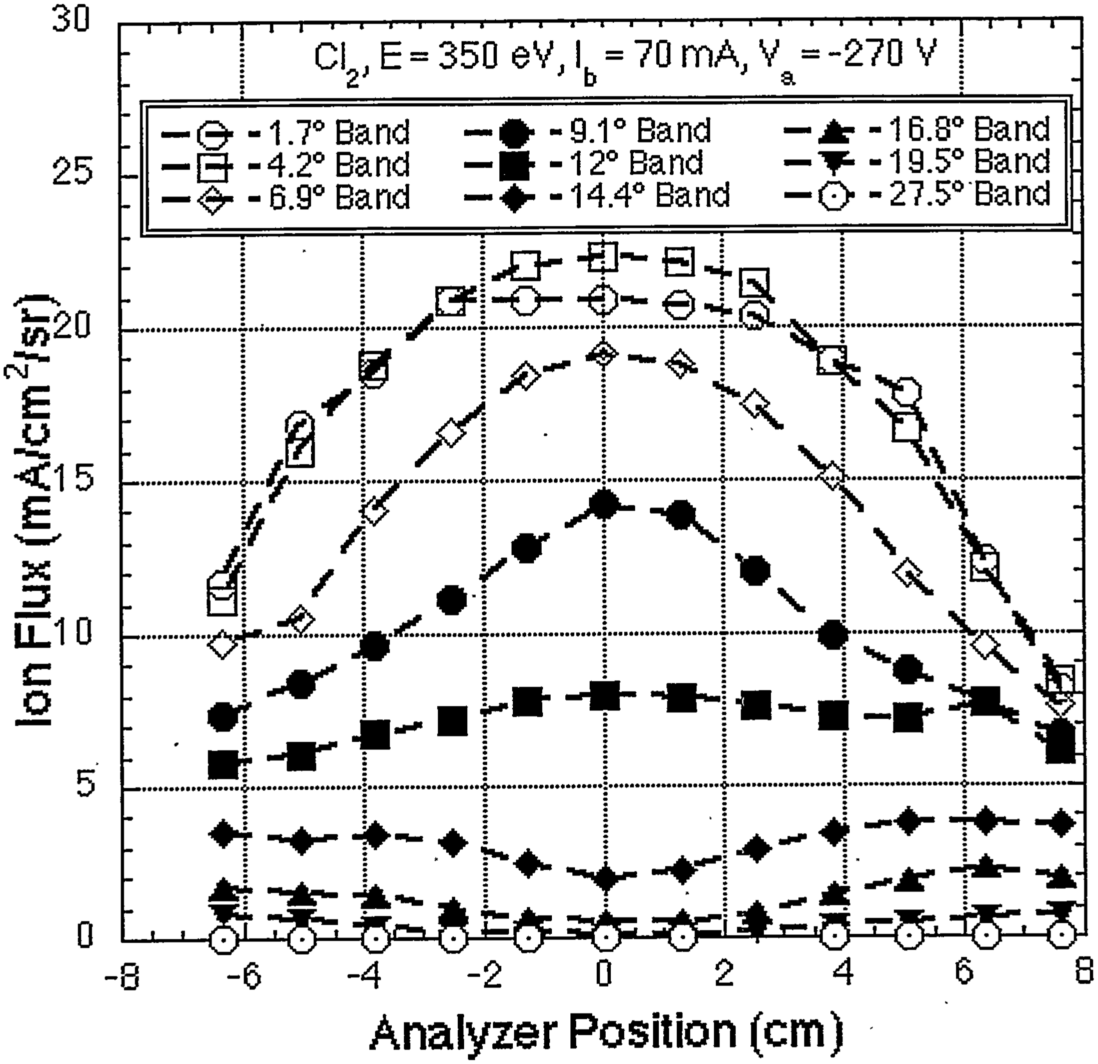

Cl_2, E = 350 eV, I_b = 70 mA, V_a = -270 V
1.7° Band
4.2° Band
6.9° Band
9.1° Band
12° Band
14.4° Band
16.8° Band
19.5° Band
27.5° Band
Ion Flux (mA/cm^2/sr)
Analyzer Position (cm)
0
5
10
15
20
25
30
-8
-6
-4
-2
0
2
4
6
8

Fig 5

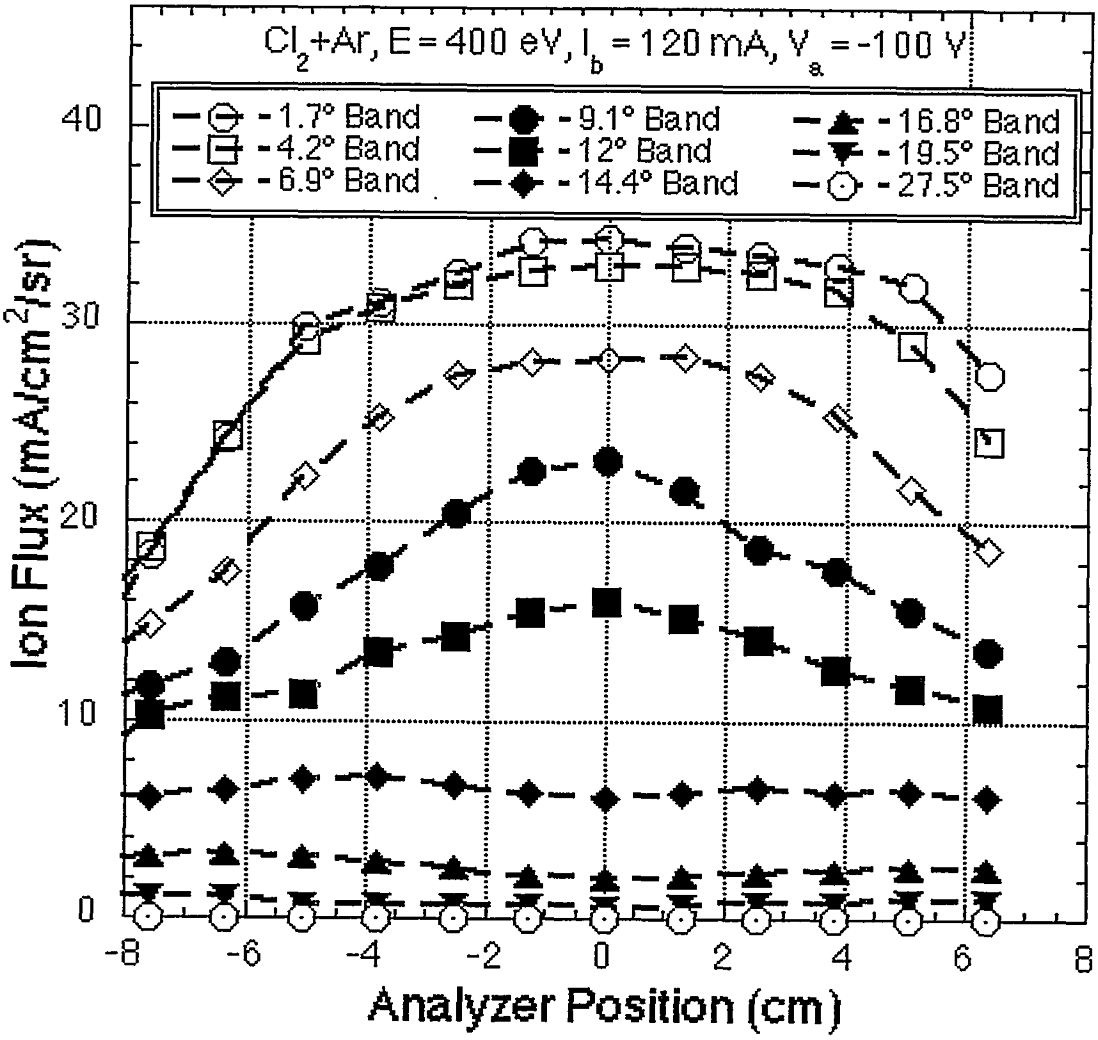
Cl_2+Ar, E=400 eV, I_b=120 mA, V_a=-100 V
-1.7° Band
-4.2° Band
-6.9° Band
-9.1° Band
-12° Band
-14.4° Band
-16.8° Band
-19.5° Band
-27.5° Band
Ion Flux (mA/cm^2/sr)
0
10
20
30
40
-8
-6
-4
-2
0
2
4
6
8
Analyzer Position (cm)

Fig. 6

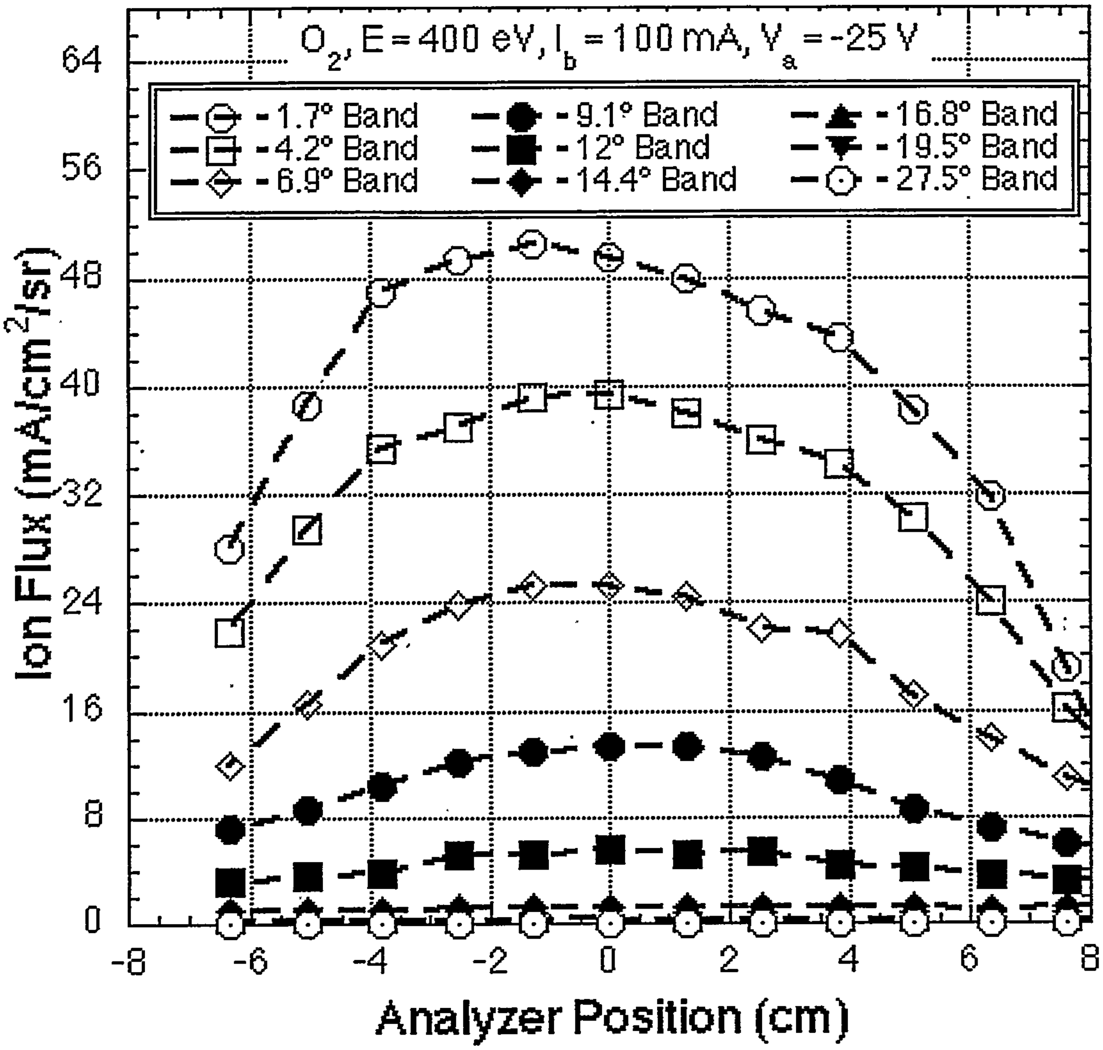
O_2, E = 400 eV, I_b = 100 mA, V_a = -25 V
1.7° Band
4.2° Band
6.9° Band
9.1° Band
12° Band
14.4° Band
16.8° Band
19.5° Band
27.5° Band
Ion Flux (mA/cm^2/sr)
0
8
16
24
32
40
48
56
64
-8
-6
-4
-2
0
2
4
6
8
Analyzer Position (cm)

Fig 7

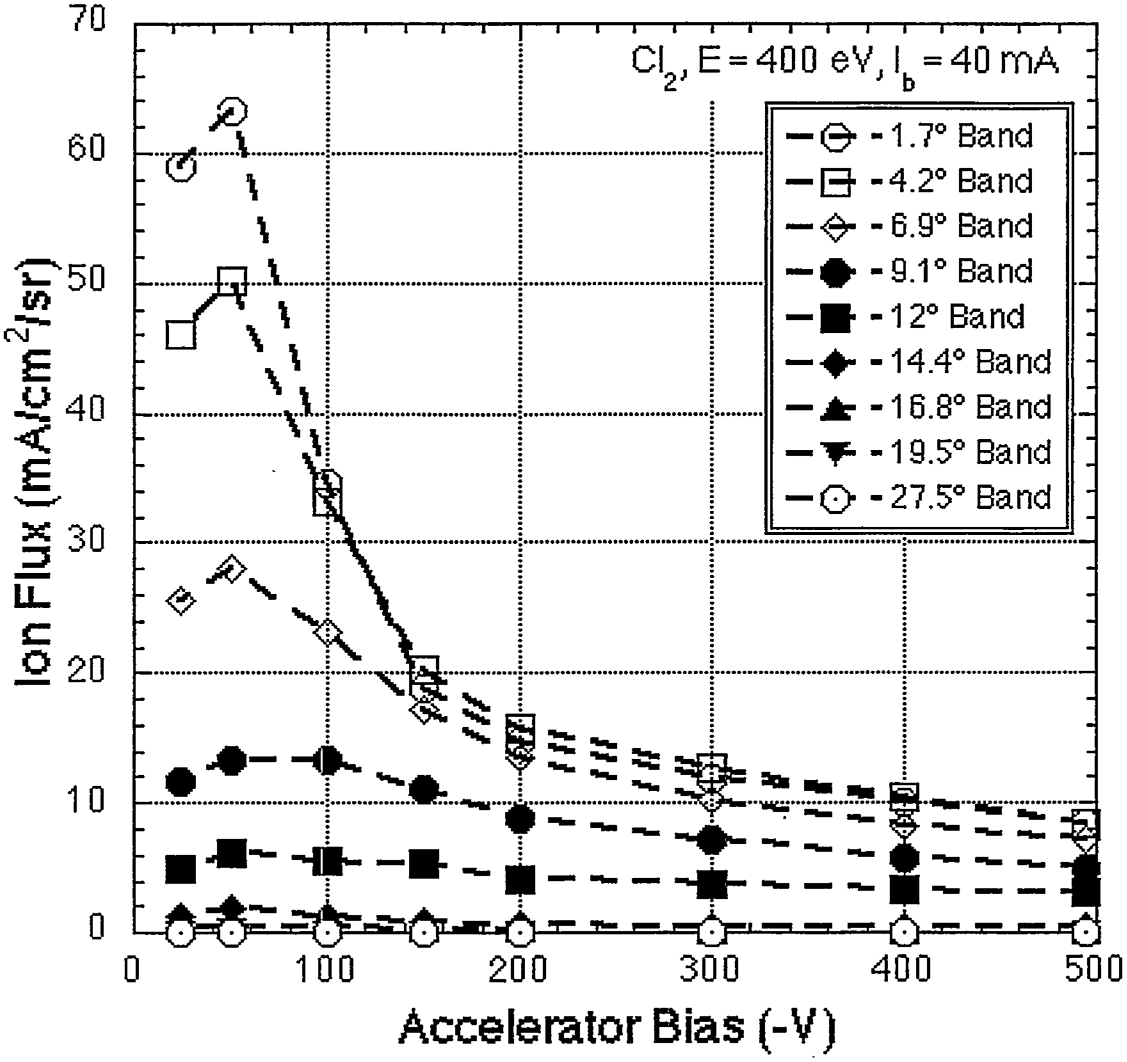
Cl2, E = 400 eV, Ib = 40 mA
1.7° Band
4.2° Band
6.9° Band
9.1° Band
12° Band
14.4° Band
16.8° Band
19.5° Band
27.5° Band
Ion Flux (mA/cm2/sr)
0
10
20
30
40
50
60
70
Accelerator Bias (-V)
0
100
200
300
400
500

Fig 8

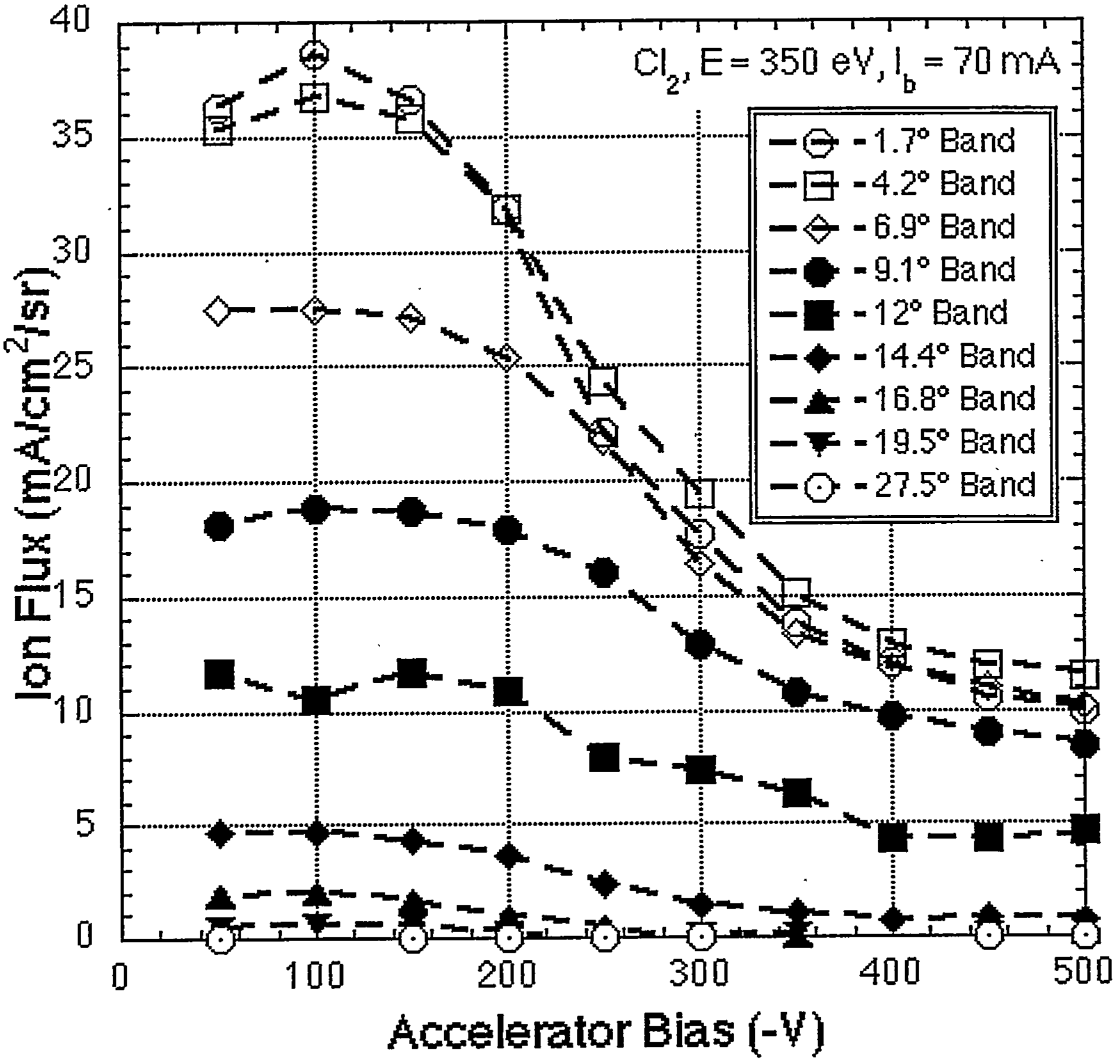

Cl_2, E = 350 eV, I_b = 70 mA
Ion Flux (mA/cm^2/sr)
Accelerator Bias (-V)
0
100
200
300
400
500
0
5
10
15
20
25
30
35
40
1.7° Band
4.2° Band
6.9° Band
9.1° Band
12° Band
14.4° Band
16.8° Band
19.5° Band
27.5° Band

Fig 9

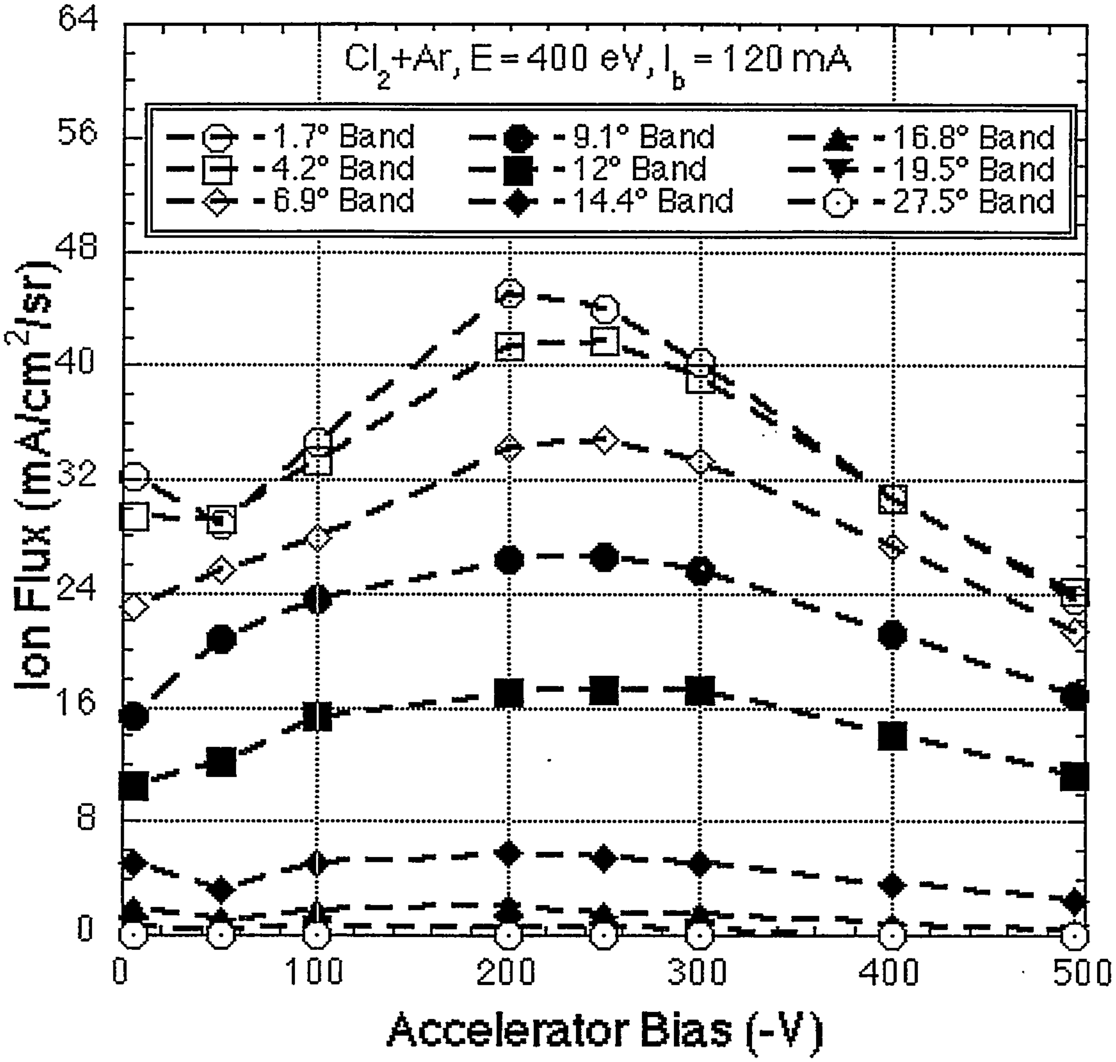
Cl_2+Ar, E = 400 eV, I_b = 120 mA
1.7° Band
4.2° Band
6.9° Band
9.1° Band
12° Band
14.4° Band
16.8° Band
19.5° Band
27.5° Band
Ion Flux (mA/cm²/sr)
Accelerator Bias (-V)
0
8
16
24
32
40
48
56
64
0
100
200
300
400
500

Fig 10

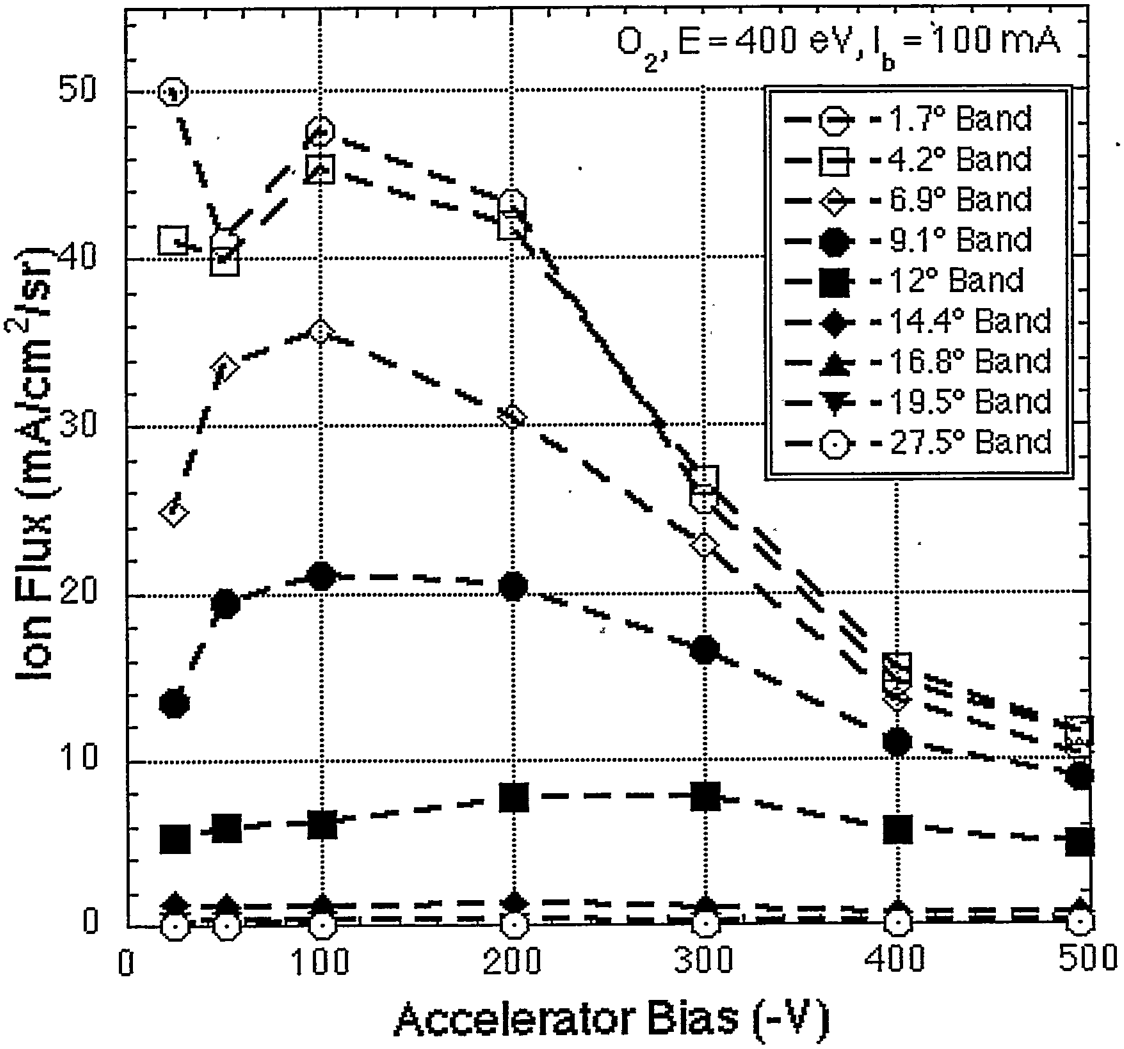
O_2, E = 400 eV, I_b = 100 mA
1.7° Band
4.2° Band
6.9° Band
9.1° Band
12° Band
14.4° Band
16.8° Band
19.5° Band
27.5° Band
Ion Flux (mA/cm^2/sr)
0
10
20
30
40
50
0
100
200
300
400
500
Accelerator Bias (-V)

Fig 11

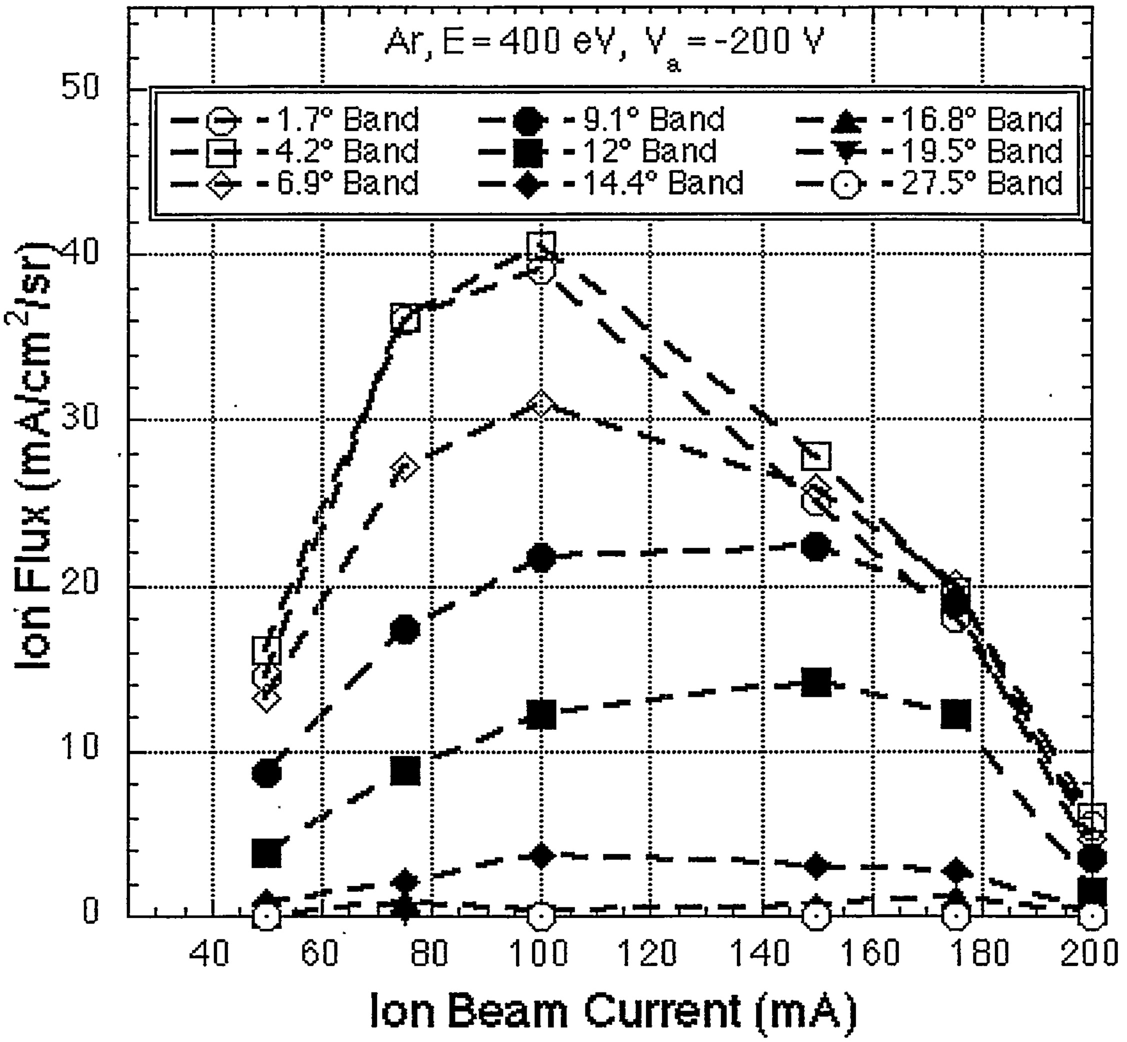
Ar, E=400 eV, V$_a$=-200 V
1.7° Band
4.2° Band
6.9° Band
9.1° Band
12° Band
14.4° Band
16.8° Band
19.5° Band
27.5° Band
Ion Flux (mA/cm^2/sr)
0
10
20
30
40
50
40
60
80
100
120
140
160
180
200
Ion Beam Current (mA)

Fig 12

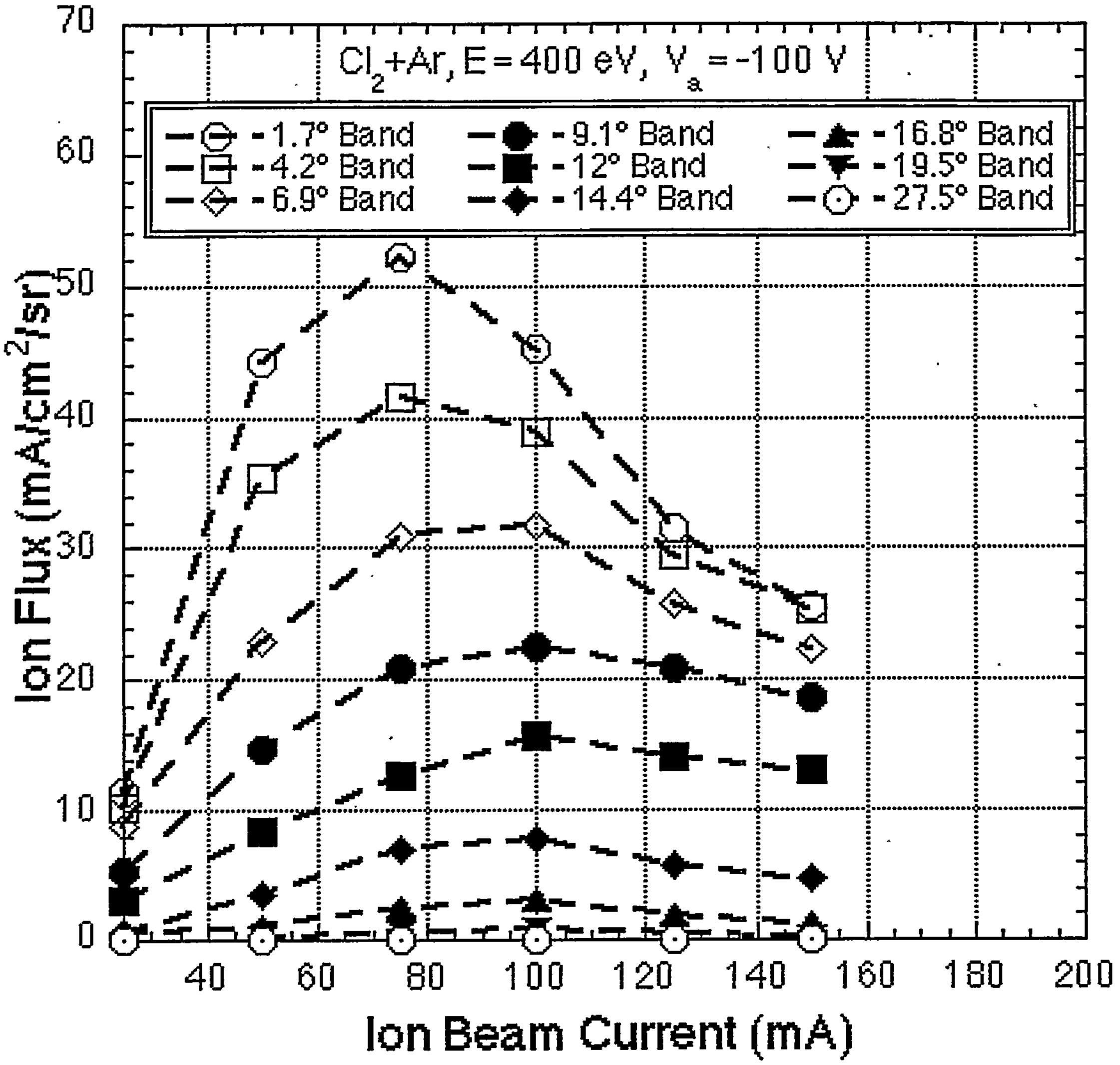

Cl$_2$+Ar, E=400 eV, V$_a$=-100 V
1.7° Band
4.2° Band
6.9° Band
9.1° Band
12° Band
14.4° Band
16.8° Band
19.5° Band
27.5° Band
Ion Flux (mA/cm^2/sr)
0
10
20
30
40
50
60
70
40
60
80
100
120
140
160
180
200
Ion Beam Current (mA)

Fig 13

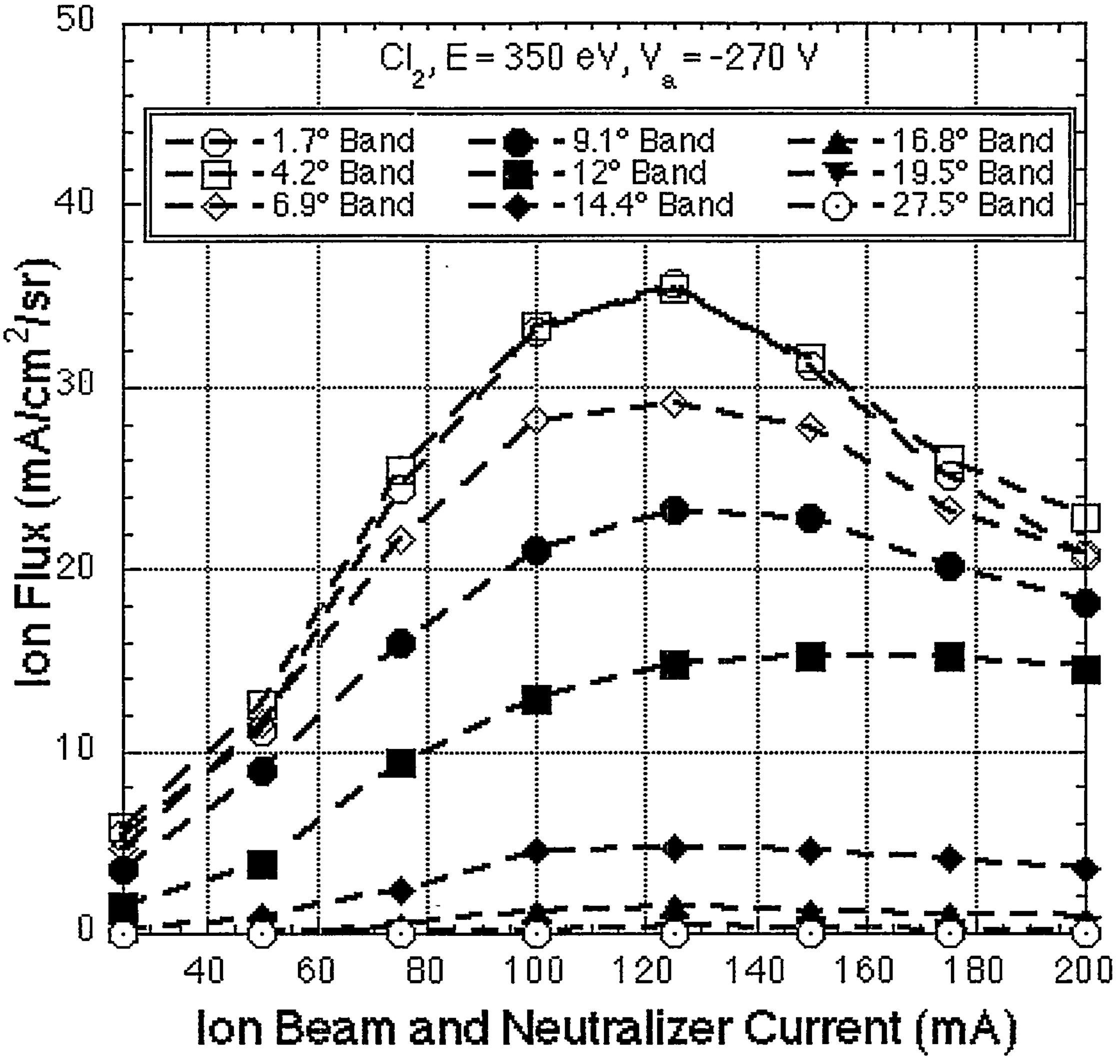
Cl_2, E = 350 eV, V_a = -270 V
1.7° Band
4.2° Band
6.9° Band
9.1° Band
12° Band
14.4° Band
16.8° Band
19.5° Band
27.5° Band
Ion Flux (mA/cm^2/sr)
0
10
20
30
40
50
40
60
80
100
120
140
160
180
200
Ion Beam and Neutralizer Current (mA)

Fig 14

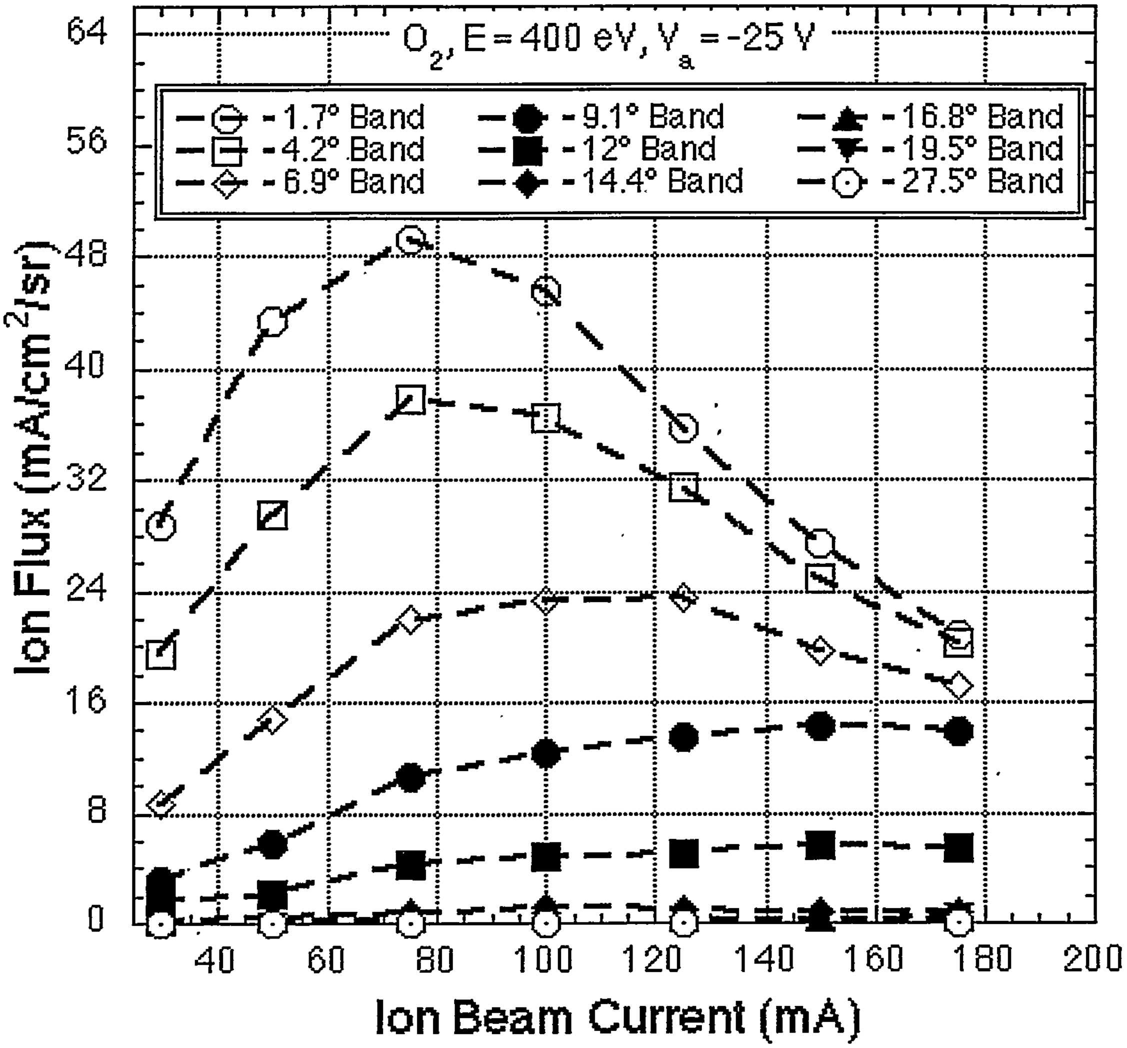

O_2, E=400 eV, V_a=-25 V
1.7° Band
4.2° Band
6.9° Band
9.1° Band
12° Band
14.4° Band
16.8° Band
19.5° Band
27.5° Band
Ion Flux (mA/cm²/sr)
0
8
16
24
32
40
48
56
64
Ion Beam Current (mA)
40
60
80
100
120
140
160
180
200

Fig 15

Appendix D

High-Aspect-Ratio Nanophotonic Components Fabricated by Cl_2 RIBE.

To be published in Journal of Vacuum Science and Technology

Formerly entitled : Influence of Ion Beam Divergence and Chamber Pressure on High-Aspect Ratio Nanophotonic Components by Cl_2 RIBE

Presented at the 43rd International Conference on Electron, Ion, and Photon Beam Technology & Nanofabrication
Marco Island, FL, USA, June 1-4, 1999

High-Aspect-Ratio Nanophotonic Components Fabricated by Cl_2 RIBE.

W. J. Zubrzycki, G. A. Vawter, and J. R. Wendt
Sandia National Laboratories, P.O. Box 5800, Albuquerque, NM 87185-0603

ABSTRACT

We describe highly anisotropic reactive ion beam etching of nanophotonic structures in AlGaAs based on the ion beam divergence angle and chamber pressure. The divergence angle is shown to influence the shape of the upper portion of the etch while the chamber pressure controls the shape of the lower portion. Deeply etched distributed Bragg reflectors are etched to an aspect ratio of 8:1 with 100 nm trench widths. The profile of the grating etch is straight with smooth sidewalls, flat bottoms, and squared corners. Two-dimensional photonic crystal post arrays are fabricated with smooth and vertical sidewalls, with structures as small as 180 nm in diameter and 2.0 μm in height.

INTRODUCTION

Control of semiconductor etch profiles are necessary for the realization of periodic nano-photonic reflecting structures[1]. In this paper, highly efficient square wave shaped distributed Bragg reflectors (DBR's) are fabricated in $Al_{0.4}Ga_{0.6}As$ by etching deep trenches into a ridge waveguide. The grating trench measures 100 nm wide and 800 nm deep across a 2.0 μm wide ridge waveguide.

Several authors present theories describing the surface reactions occurring during a chlorine based (Al, Ga)As etch[2, 3, 4, 5]. Each describes a surface film or residue, composed of $GaCl_x$, $AsCl_x$, or AlO_3 that forms during the etch process and must be removed, typically by sputtering, before any additional semiconductor may be etched. In this work, highly anisotropic Cl_2 reactive-ion-beam etching (RIBE) is described wherein the lateral etch rate is matched to the lateral deposition (residue) rate using the divergence angle and the chamber pressure as control variables. The ion beam divergence angle influences the ion trajectory and etch rate, controlling the shape of the upper portion of the etched structure. The chamber pressure affects the mean-free path length and chemical etch efficiency and is used to control the shape of the bottom of the etched structure. Using these methods we have etched 100 nm line-and-space grating teeth nearly 1 μm deep into a $Al_{0.4}Ga_{0.6}As$ waveguide for photonic integrated circuits and devices.

BACKGROUND

The RIBE system is equipped with an inductively-coupled plasma (ICP) source as shown schematically in Figure 1. The desired etch gas flows into the discharge chamber at the base of the ion source. The discharge chamber consists of a quartz confinement cylinder with a water cooled RF antenna coiled around the cylinder. Ions are extracted by the potential difference between the source and the grounded sample stage. Dual graphite grids provide a means to control the divergence of the ion beam. The grid set includes two 15 cm diameter graphite disks with 1.2 mm diameter holes spaced 4.0 mm apart and placed in a uniform hexagon pattern. The grid separation is 0.7 mm. The screen grid is located towards the source and the accelerator grid is located towards the etch sample. The screen grid and discharge chamber are held at the beam potential while the accelerator grid is separately biased to control the beam divergence. The sample stage is located 35 cm below the grids. Typical beam voltages used to etch photonic devices range from 300 V to 500 V, beam currents from 40 mA to 120 mA, and accelerator bias of -50 V to -480 V.

In this system, the etch chamber has a background pressure into the low 10^{-8} Torr range. Typical chamber pressures during an etch range from 0.15 mTorr to 0.45 mTorr. Chamber pressures less than 0.25 mTorr are considered low pressure and greater than 0.3 mTorr are considered high pressure etches.

The Divergence Angle

The divergence angle is defined as the half angle of a beamlet exiting an accelerator grid hole containing ninety-five percent of the ion flux[6]. The beam divergence is a function of accelerator voltage, beam energy, and total current, all of which affect the etch profile and the etch rate. The relationship between the ion source parameters and divergence angle[7] is calculated theoretically and shown in Figure 2.

The etch rate at a point on the sample stage is determined by the current density of ions incident on that point. The beam current influences the etch rate by defining the ion current density exiting the grid, hence, a direct relationship to the flux of ions at a point on the sample. Given a constant beam current, (constant flux of ions exiting the grid) varying the divergence angle via the accelerator voltage also affects the etch rate as shown in Figure 3. Although the current density exiting the grid remains constant, varying the divergence angle changes the current density at a point on the sample stage[8]. Smaller accelerator voltages reduce the divergence angle. This affects the flux of ions at the sample by decreasing the width of each beamlet, concentrating the ions into a smaller area, thus increasing the current density at a point on the sample. Increasing the accelerator voltage increases the divergence angle. A larger divergence angle increases the width of each beamlet, distributing the flux of ions onto a larger area, thus decreasing the current density of a point on the sample. Figure 3 provides experimental data showing a decrease in etch rate with increasing accelerator voltage which implies a decreased ion current density at a point on the sample.

The Incident Angle

The incident angle is defined as the angle from normal of incoming ions at a point on the sample. Incident angles were determined with a model that sums the contribution from each grid hole, assuming a Gaussian ion distribution[9]. Figure 4 shows the distribution of incident angles from the model for divergence angles of 7, 14, and 24 degrees. The 7 degrees divergence curve shows a large concentration of ions with near-normal incidence (full-width-half-maximum spread from 1.5 to 7 degrees). As the divergence angle increases, the concentration of ions with near-normal incidence decreases and ions with larger incident angles are more prevalent.

The Chamber Pressure

Two processes dominate the removal of material during a RIBE plasma etch: i.) sputter etch and ii.) chemical etch. The kinetic (sputter) and chemical etch components are combined to define the sputter yield, the overall ratio of atoms removed from the surface to incident ions. Sputter etching dominates at lower pressures and lower temperatures. The chemical etch component increases as the temperature and pressure increase[5, 10]. The sputter etch removes material by the physical impact of ions on the semiconductor surface. The chemical etch process utilizes a corrosive gas, such as chlorine, which reacts with the semiconductor surface and directly removes material or forms a volatile product (film or residue) that is removed by sputtering. In this work, the chamber pressure (chlorine partial pressure) was used to control the chemical etch component.

The chamber pressure is controlled by the gas flow rate and a throttle valve located between the chamber and vacuum pump. Increasing the chamber pressure with an increase in gas flow while maintaining a constant beam current and throttle valve setting (constant density of ionized species) increases the ratio of non-ionized to ionized chlorine (Cl_2/Cl_x^+). A greater density of non-ionized Cl_2 atoms in the chamber increases the surface coverage of the reactive gas. As a result, the formation rate of the chemically reacted species $AsCl_x$ and $GaCl_x$ increases, improving the sputter yield. Increasing the chamber pressure with the throttle valve while maintaining a constant beam current and gas flow maintains the Cl_2/Cl_x^+ ratio from the source, but, increases the residence time and total density of species in the chamber. In both cases, a greater density of charge neutral chlorine in the chamber increases the Cl_2 coverage which increases the lateral and vertical etch rate.

EXPERIMENT

The grating process begins with the deposition of a layer of SiO_2 (8000 Å), followed by 2000 Å of Polymethylmethacrylate (PMMA), direct-write e-beam resist. The grating patterns are written using a JEOL JBX-5FE direct write electron beam lithography system. After exposure, the PMMA is developed for 60 seconds in a solution of Methyl Isobutyl Ketone:Isopropyl Alcohol (MIBK:IPA) diluted 1:3. A bimetal layer comprised of 50 Å of Cr and 500 Å of Ni is evaporated using the PMMA as a lift-off mask. Following the Cr/Ni liftoff, the remaining metal is used as a mask to pattern the SiO_2 in an RIE system. The sample is loaded into the RIBE and pumped to approximately $5x10^{-8}$ Torr prior to the grating etch.

The RIBE characterization involves determining the divergence angle and chamber pressure that produces a highly anisotropic sidewall etch with flat bottoms in the grating trenches. A matrix of accelerator voltages and beam currents (divergence angle, see Figure 2) and chamber pressures are examined. Divergence angles ranging from 14° to 24° are examined by varying the beam current from 25 mA to 100 mA and accelerator bias from -75 V to -460 V. The chamber pressure varies from 0.15 mTorr to 0.45 mTorr while the beam voltage remained constant at 400 V.

RESULTS AND DISCUSSION

A small divergence angle was found to erode the mask material resulting in an angled or inverted V shaped grating mask, producing a tapered etch profile. The ions with small incidence angles graze the sidewalls and are not efficient in removing sidewall material. The tapered etch is shown in Figure 5 where an etch with a beam current of 50 mA and accelerator bias of -50 V, (resulting in a divergence of 12.5°) was used. This same milling effect is observed for large divergence angles (21°) at higher beam currents (100 mA). Although the large divergence angle decreases the flux of near normal incidence ions (compared to a small divergence angle), the increase in ion flux caused by the high beam current dominates the etch, resulting in mask erosion and a tapered etch profile.

A low pressure etch reduces the density of neutrals in the chamber, resulting in decreased surface coverage, hence a decrease in the $AsCl_x$ and $GaCl_x$ residue formation. As a result, the sputter yield and sidewall etch rate are reduced. This is observed experimentally in the lateral etch rate at the bottom of the trench where the low pressure etch produces a V shaped etch, see Figure 6 (a). Increasing the chamber pressure enhances the $AsCl_x$ and $GaCl_x$ formation (chemical etch component) resulting in an increased sputter yield and lateral and vertical etch rates. The lateral etch rate was used to obtain the sidewall profile while the etch time was varied to account for changes in vertical etch rates. Typically, too much pressure-induced lateral etching tends to undercut the mask as shown in Figure 6 (b).

The etch matrix provides an understanding of the effects of the chamber pressure and divergence angle on the nanostructure profile. The final etch parameters match the lateral etch rate to the lateral residue formation rate, resulting in a grating trench with straight sidewalls, flat bottoms, and squared corners as shown in the cross-sections of Figure 7(a) and (b). Figure 7 (a) is a cleave through the grating region perpendicular to the grating tooth and Figure 7 (b) is a cleave through a grating trench, parallel to the grating teeth. The square-wave-shape etch results from a divergence angle of 24° and chamber pressure of 0.31 mTorr.

The divergence angle of 24° is produced by a 40 mA beam current, -460 V accelerator bias, and 400 V beam voltage. The combination of a low beam current and large divergence angle resulted in negligible mask erosion, maintaining vertical sidewalls on the upper portion of the etch. Figure 7 (a) shows remaining mask on three grating teeth, after an incomplete mask removal process. The remaining mask shows no degradation caused by small divergence angle erosion. (The web between the teeth is a very thin film of remaining un-etched waveguide on the far side of the grating.)

The grating etch was applied to the fabrication of a two-dimensional photonic crystal[1,11]. The photonic crystal device is a two-dimensional array of posts located between two ridge waveguides. The required etch characteristics include maintaining the post diameter and perfectly vertical and smooth sidewalls. The post mask consists of 1.0 µm of hardbaked photoresist (250° C) with dots patterned by direct-write electron beam lithography. PMMA was used as a lift-off mask for a bimetal layer consisting of 50 Å of titanium and 500 Å of nickel. Samples were loaded into the RIBE and pumped into the 10^{-8} Torr region. The hardbaked PR was etched in the RIBE system with an anisotropic oxygen etch followed by the chlorine post etch.

Post etch dynamics are similar to the gratings; the divergence angle influenced the top portion of the post and the chamber pressure affected the bottom of the post. The primary difference between the grating and post etch is the depth. Initially, a higher beam current process was examined based on the faster etch rate. The higher beam current process was examined fully, concluding with relatively straight post sidewalls, but, accelerated mask erosion introduced defects in the sidewalls, particularly in the upper portion. The large divergence angle, high-pressure grating etch which gave the results of Figure 7, produced tapered posts, nearly pinched-off at the bottom. Reducing the chamber pressure resulted in a successful post etch, see Figure 8. The post etch parameters are a 400 V beam voltage, 40 mA beam current, -460 V accelerator bias, 0.25 mTorr chamber pressure, 24° divergence angle, and a resulting etch rate of 18 nm/min.

SUMMARY

We have characterized the large ion beam divergence angle region of parameter space in a RIBE system. In an ion beam assisted etch system[12], highly anisotropic structures have been etched with a small divergence angle (<5°) using a small ion source and large sample-source spacing. In contrast, in our broad beam (15 cm dia.) RIBE system, the divergence angle has a significant influence on the profile. In such a broad ion beam system, the use of the accelerator grid bias to control and actually enhance beam divergence is critical to obtain high-aspect-ratio nanostructures. The large divergence angle region of parameter space predictably influences the upper portion of the etched structure while the chamber pressure influences the lower portion of the etch. The combined effects produced nanostructures with vertical and smooth sidewalls.

Sandia is a multiprogram laboratory operated by Sandia Corporation, a Lockheed Martin Company, for the United States Department of Energy under Contract DE-AC04-94AL85000.

REFERENCES

1 W. J. Zubrzycki, "*Fabry-Perot waveguide modulator with nanophotonic distributed mirrors,*" Thesis

Dissertation, Drexel University, Philadelphia, PA, June 1999.

2 M. Balooch, D. R. Olander, and W. J. Siekhaus, J. Vac. Sci. & Tech. B4(4), 794-805 (1986).

3 J. H. Ha, E. A. Ogryzlo, and S. Polyhronopoulos, J. Chem. Phys. 89(5) 2844-2847 (1988).

4 R. J. Davis and E. D. Wolf, J. Vac. Sci. & Tech. B8(6), 1798-1803 (1990).

5 K. Asakawa and S. Sugata, J. Vac. Sci. & Tech. B3(1), 402-405 (1985).

6 T. Jolly, *Handbook of Ion Sources*, Ed: B. Wolf, (CRC Press, 1995) pp. 209-237.

7 G. A. Vawter, "Ion beam etching of compound semiconductors," in "*Advanced plasma processing techniques*," Ed: S. Pearton and R. Shul, (Springer-Verlag, to be published.)

8 G. A. Vawter, J. R. Woodworth, and W. J. Zubrzycki, J. Vac. Sci. Tech. (To be published, same issue as this article.) (1999).

9 D. Korzec, K. Schmitz, and J. Engemann, J. Vac. Sci. & Tech. B6(1), 263 (1988).

10 T. Tadokoro, F. Koyama, and I, Kenichi, Jap. J. of Appl. Phy., Part 1, 27(3): 389-92 (1988).

11 S. Y. Lin, G. A. Vawter, J. R. Wendt, W. J. Zubrzycki, H. Hou, and B. E. Hammons, LEOS (San Francisco, CA) WA2, vol. 2, pp. 5, (1997).

12 G. A. Lincoln, M. W. Geis, S. Pang, and N. N. Efremow, J. Vac. Sci. & Tech. B1(4), 1043-6 (1983).

FIGURE CAPTIONS

Figure 1: Schematic representation of RIBE plasma source.

Figure 2: Divergence angles in RIBE for 400 V beam voltage. Angles are in degrees and total current includes beam and accelerator current.

Figure 3: Experimental large area etch rate of AlGaAs as a function of accelerator voltage. Fixed parameters were: V_B=400 V, I_B=50 mA, Pr=0.15 mTorr, Cl_2=3.0 sccm.

Figure 4: Ion density as a function of incident angle at the center of the sample stage. Partial results from RIBE GRID modeling program with vertical incidence taken as 0°. Grid hole diameter=1.2 mm, grid hole spacing=4.0 mm, grid diameter=15 cm, holes were placed in a uniform hexagon pattern.

Figure 5: Erosion of mask by small divergence angle. V_B = 400 V, I_B = 50 mA, V_{acc} = -50 V, Divergence Angle = 12.5°.

Figure 6: Controlling lateral etch with chamber pressure. The chamber pressure in (a) was 0.25 mTorr and

increased to 0.3 mTorr in (b). Remaining etch parameters are: beam voltage = 400 V, beam current = 30 mA, accelerator voltage = -425 V.

Figure 7: Vertical sidewall, flat bottom grating etch shown in (a). Grating pitch of 200 nm and fifty percent duty cycle resulted in a trench etch width of 100 nm. The etch depth measured 710 nm. A high pressure etch, 0.31 mTorr, was obtained with a low Cl_2 gas flow of 4.0 sccm and a partially closed throttle valve. The etch rate of the trench is 22 nm/min. The three teeth on the left show remaining etch mask after incomplete removal process. Shown in (b) is a cross-section of a deep etched grating cleaved parallel to the grating trench, showing the uniformity of the bottom.

Figure 8: Shown in (a) is a cleaved cross-section of the post array. The post diameter is 180 nm and the etch depth is 2.0 μm. The white outline on the left displays the post shape. In (b), the post array forms a photonic crystal reflector.

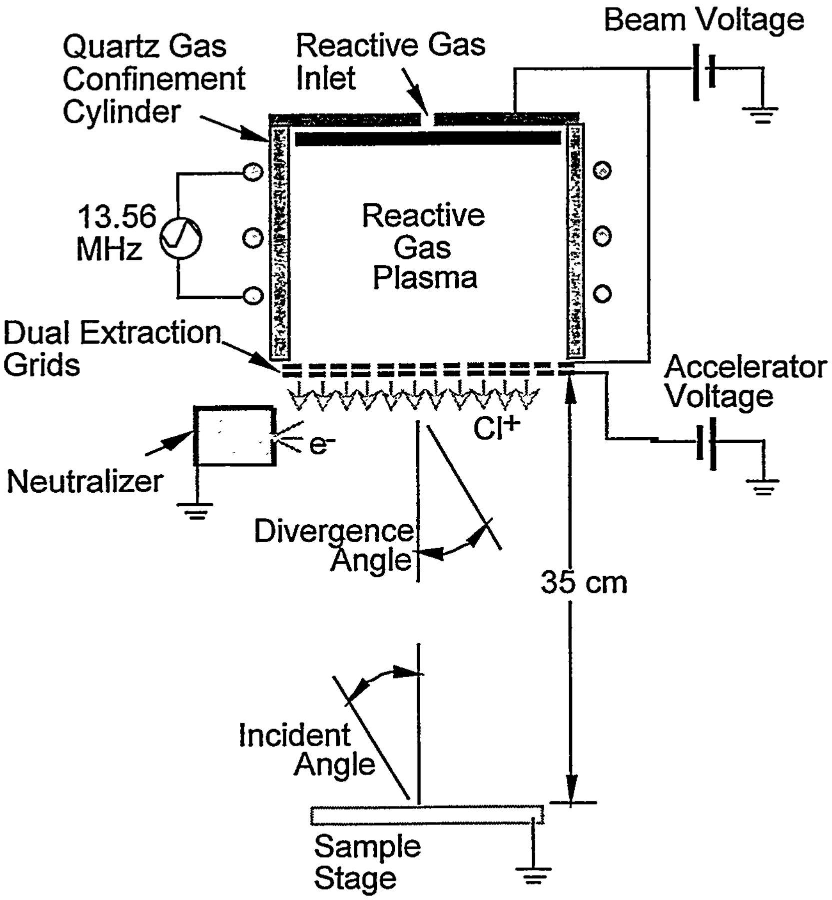
Beam Voltage
Quartz Gas Confinement Cylinder
Reactive Gas Inlet
13.56 MHz
Reactive Gas Plasma
Dual Extraction Grids
Accelerator Voltage
e-
Cl+
Neutralizer
Divergence Angle
35 cm
Incident Angle
Sample Stage

Fig 1

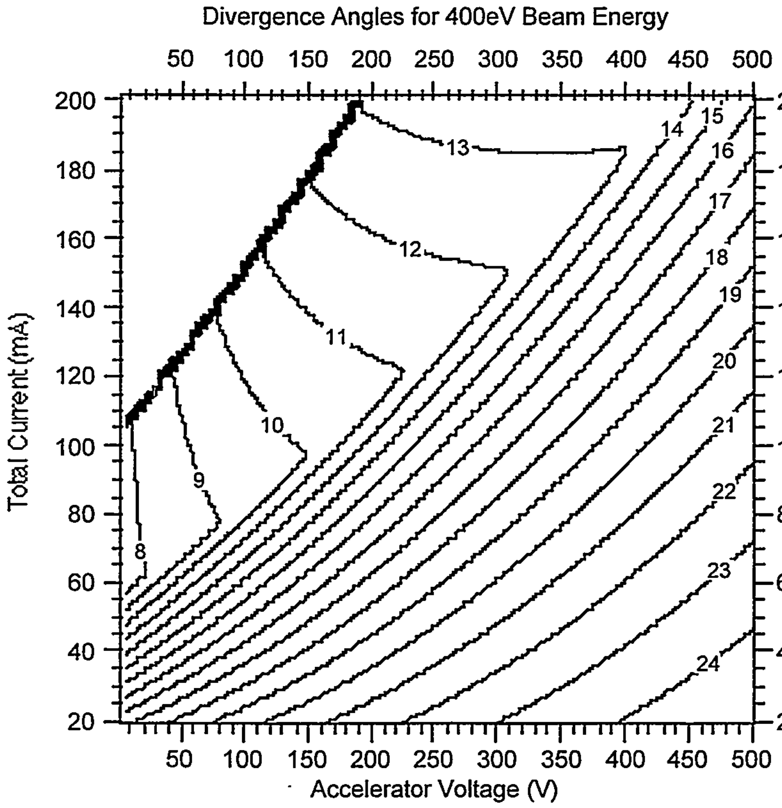
Divergence Angles for 400eV Beam Energy
50 100 150 200 250 300 350 400 450 500
200
180
160
140
120
100
80
60
40
20
Total Current (mA)
Accelerator Voltage (V)
8
9
10
11
12
13
14
15
16
17
18
19
20
21
22
23
24

Fig 2

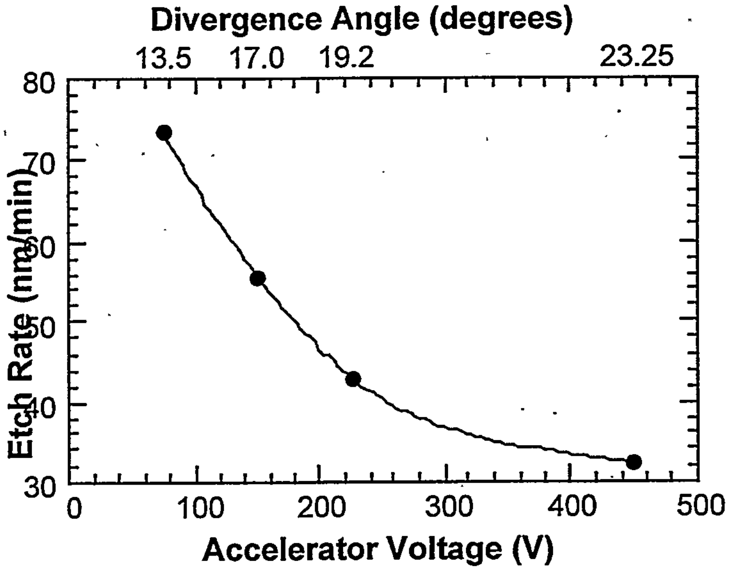
Divergence Angle (degrees)
13.5
17.0
19.2
23.25
80
70
60
50
40
30
Etch Rate (nm/min)
0
100
200
300
400
500
Accelerator Voltage (V)

Fig 3

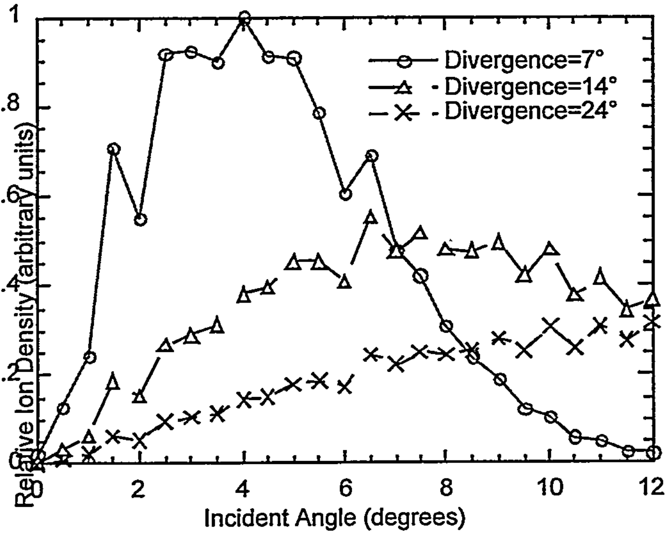

Relative Ion Density (arbitrary units)
Incident Angle (degrees)
0
0.2
0.4
0.6
0.8
1
0
2
4
6
8
10
12
Divergence=7°
Divergence=14°
Divergence=24°

Fig 4

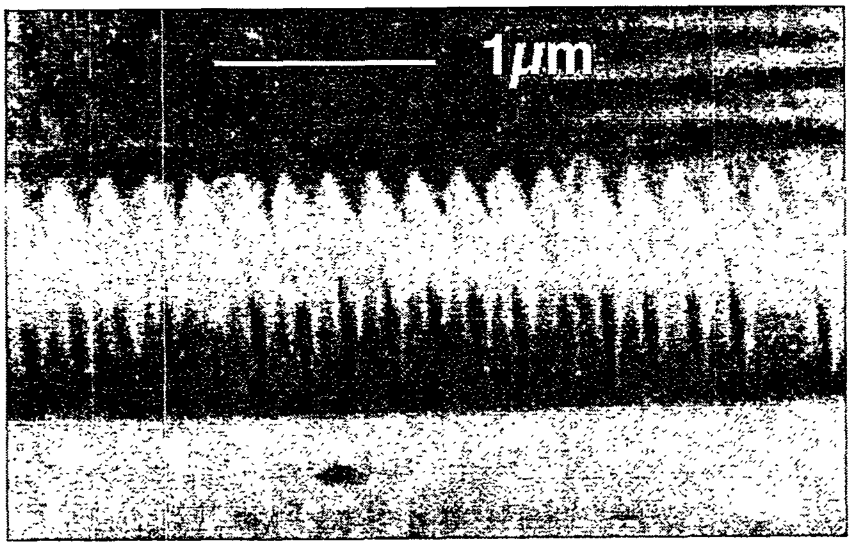
1μm

Fig 5

QuickTime™ and a
decompressor
are needed to see this picture.

(a)

QuickTime™ and a
decompressor
are needed to see this picture.

(b)

Fig 6

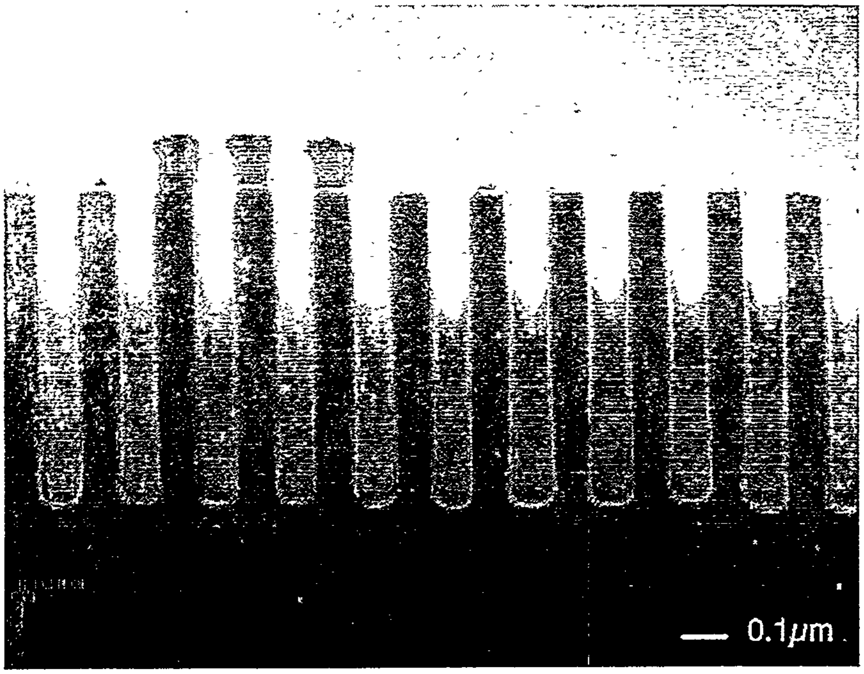

(a)

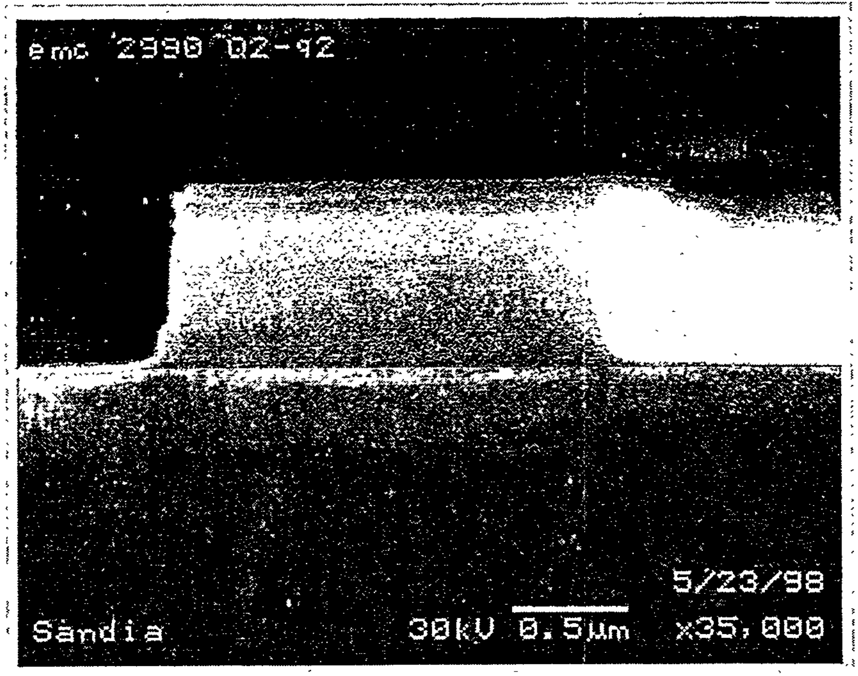

(b)

Fig 7

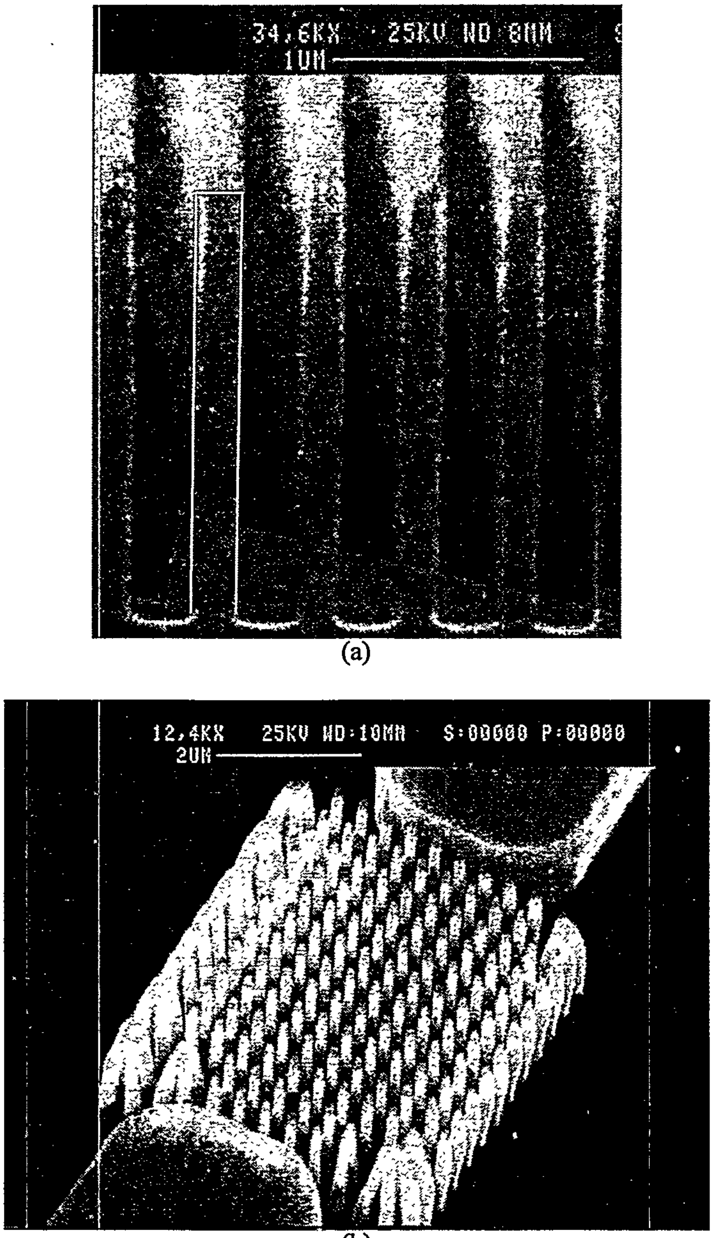

(a)

(b)

Fig 8

SAND Report Distribution list:

3	MS 0603	Carol I. Ashby, 1711
1	MS 0603	Peter Esherick, 1711
1	MS0603	G. Allen Vawter,1711
1	MS 0603	Walter J. Zubrzycki, 1711
1	MS 0603	Thomas E. Zipperian, 1713
1	MS 601	William G. Breiland, 1126
1	MS 0601	Larry A. Bruskas, 1126
1	MS 0601	Jeffrey Y. Tsao, 1126
1	MS 1423	Joseph R. Woodworth, 1128
1	MS 1423	Gregory A. Hebner, 1128
1	MS 1423	Gerald N. Hays, 1128
1	MS 0188	LDRD Office, 4001
1	MS 9018	Central Technical Files, 8940-2
2	MS 0899	Technical Library, 4916
1	MS 0612	Review & Approval Desk 4912 for DOE/OSTI
1	MS 0161	Patent and Licensing Office, 11500